Composite Structures 337 (2024) 118037

Contents lists available at ScienceDirect

Composite Structures

journal homepage: www.elsevier.com/locate/compstruct

Semi-analytical approach for curved masonry pillars reinforced with FRCM

Gabriele Milani [a,*], Ernesto Grande [b], Tommaso Rotunno [c], Mario Fagone [d]

[a] Department of Architecture, Built Environment and Construction Engineering, Politecnico di Milano, Piazza Leonardo da Vinci 32, 20133 Milano, Italy
[b] Department of Civil and Mechanical Engineering, University of Cassino and Southern Lazio, via G. Di Biasio 43, 03043 Cassino, Italy
[c] Department of Architecture (DiDA), University of Florence, Piazza Brunelleschi 6, 50121 Florence, Italy
[d] Department of Civil and Environmental Engineering (DICeA), University of Florence, Via di S. Marta, 3, 50139 Florence, Italy

ARTICLE INFO

Keywords:
Semi-analytical model
FRCM-to-substrate shear bond tests
Curved substrates
Masonry
debonding of FRCM from substrate
Matrix cracking

ABSTRACT

The paper presents a semi-analytical approach for the study of the debonding phenomenon of Fiber Reinforced Cementitious Matrix (FRCM) systems externally applied to curved masonry pillars. One of the main features of the approach consists of considering the strengthening system composed by three separated components: external mortar layer, central fiber net and internal mortar layer. These components, assumed subjected to a longitudinal state of stress, interact one each other through tangential stresses developing at the level of zero-thickness interfaces. Regarding the latter, a tri-linear shear stress-slip relationship is assumed to account for a first elastic phase, a second phase exhibiting linear softening and a third phase with a possible non-null residual strength. Since in case of curved substrates, by equilibrium, normal stresses at the interfaces between fiber and matrix arise, which modify the peak tangential resistance and the ductility, a classic Mohr-Coulomb criterion is introduced in the approach. Additionally, the central fiber net progressively transfers along the bond length the force applied at its loaded end by means of an elastic interface interposed between the internal mortar layer and the substrate, the latter assumed rigid and infinitely resistant. The longitudinal equilibrium equations written for the two mortar layers, suitably re-arranged considering the constitutive behavior of the layers, allow to deduce a field problem governed by six first order differential equations into six unknowns. The non-linearity is tackled by means of a recursive elastic numerical algorithm where the elastic modulus of the damaged materials is progressively dropped down, subdividing the bonded length into small portions where the material properties are assumed constant. For each element the solution of the field problem is known in closed form and the only variables to determine are the integration constants coming from the solution of the differential equation system. After a standard assemblage, all constants are derived imposing the boundary conditions at the extremes of the elements, which depend on the state of cracking of the matrix layer. The validation of the proposed approach is carried out with reference to recent experimental tests carried out by the Authors. The obtained results show the reliability of the approach to account for the influence of the curvature of the substrate on the debonding process of FRCM systems.

1. Introduction

Strengthening interventions on existing masonry structures based on the use of fiber reinforced composite materials are nowadays a current and increasing practice. In particular, reinforcements made of sheets or strips embedded into inorganic matrices (called Fiber Reinforced Cementitious Matrix, FRCM, or Textile Reinforced Matrix, TRM) externally applied to masonry substrates represent one of the most used techniques ([1–7]). Indeed, this technique, which allows for providing a system interacting with masonry by improving its capacity in tension, can be easily employed for both planar and curved substrates. The latter in particular plays a significant role in case of historical constructions where curved masonry structural elements such as arches, vaults, domes, etc., are common parts of the whole structure.

Failure modes observed for FRCM reinforcements clearly include the propagation of cracks inside the different layers.

The studies available in the literature focus the attention mainly on the local interaction mechanisms between FRCM systems and masonry substrates, and in particular they refer to a flat masonry substrate configuration ([8–30]). As existing studies emphasize, it is observed a local bond behavior where the shear-stress transfer mechanism from the reinforcement to the matrix, and then to the masonry substrate, is not only influenced by the characteristics of the involved materials

---

* Corresponding author.
E-mail address: gabriele.milani@polimi.it (G. Milani).

https://doi.org/10.1016/j.compstruct.2024.118037
Received 30 August 2023; Received in revised form 10 February 2024; Accepted 15 March 2024

Nomenclature

A	outer matrix layer
B	central fiber embedded between the two matrix layers
B_F	effective width of the central fiber
C	inner matrix layer
c_0	cohesion of the intact interface between matrix layer and central fiber
c_r	residual cohesion of the interface between matrix layer and central fiber
$d\varphi$	angle identifying the amplitude of the infinitesimal portion of the FRCM package
E_A	elastic modulus of the material composing the outer matrix layer
E_B	elastic modulus of dry fiber of the central fiber
E_C	elastic modulus of the material composing the inner matrix layer
$E_A^{(i,k)}$	elastic modulus of the infinitesimal portion (k) of the outer matrix layer at the load step (i)
$E_B^{(i,k)}$	elastic modulus of the infinitesimal portion (k) of the central fiber at the load step (i)
$E_C^{(i,k)}$	elastic modulus of the infinitesimal portion (k) of the inner matrix layer at the load step (i)
f_{tM}	tensile strength of the material composing the matrix layers
K_I	slope of the initial branch of the constitutive law of the interface between the matrix layer and central fiber
$K_{AB}^{(i,k)}$	elastic stiffnesses of the infinitesimal portion (k) of the interface between the outer matrix layer and central fiber at the load step (i)
$K_{BC}^{(i,k)}$	elastic stiffnesses of the infinitesimal portion (k) of the interface between the inner matrix layer and central fiber at the load step (i)
$K_S^{(i,k)}$	elastic stiffnesses of the infinitesimal portion (k) of the interface between the inner matrix layer and substrate at the load step (i)
$K_{AB}^{(k,i+1)}$	updated elastic stiffnesses of the infinitesimal portion (k) of the interface between the inner matrix layer and central fiber at the subsequent load step $(i+1)$
L	bonded length
L_e	length of the infinitesimal portion of the element
n_e	number of subdivisions of the bonded length accounted for the discretization
R_C	curvature radius of the interface
t_A	thickness of the outer matrix layer
t_B	thickness of the central fiber embedded between the two matrix layers
t_C	thickness of the inner matrix layer
U_A	displacement of the outer matrix layer
U_B	displacement of the central fiber embedded between the two matrix layers
U_C	displacement of the inner matrix layer
$U_B(L)$	displacement at the loaded edge of the central fiber
$U_B(0)$	displacement at the free edge of the central fiber
Δ_{Ie}	slip at the elastic limit of the interfaces between matrix layer and central fiber
Δ_{Iu}	ultimate slip of the interfaces between matrix layer and central fiber
Δ_{Ies}	slip at the elastic limit of the interfaces between matrix layer and central fiber modified by the presence of normal stresses
Δ_{Ius}	ultimate slip of the interfaces between matrix layer and central fiber modified by the presence of normal stresses
ε_{Me}	strain at the elastic limit of material composing the matrix layers
ε_{Mu}	ultimate strain of material composing the matrix layers
Φ	initial friction angle of the interfaces between matrix layer and central fiber
Φ_r	residual friction angle of the interfaces between matrix layer and central fiber
σ_A	longitudinal stresses acting on the outer matrix layer
σ_B	longitudinal stresses acting on the central fiber embedded between the two matrix layers
σ_C	longitudinal stresses acting on the inner matrix layer
$\sigma_{I,AB}$	normal stresses acting on the interface between the outer matrix layer and central fiber
$\sigma_{I,BC}$	normal stresses acting on the interface between the central fiber and inner matrix layer
τ_{AB}	tangential stress acting on the interface between the outer matrix layer and central fiber
τ'_{AB}	projection of tangential stress on the softening branch in case τ_{AB} at the end of step i exceeds τ_m
τ_{BC}	tangential stress acting on the interface between the inner matrix layer and central fiber
τ_m	shear strength of the interface between the matrix layer and central fiber modified by the presence of normal stresses
τ_r	residual shear strength of the interface between the matrix layer and central fiber modified by the presence of normal stresses
τ_S	tangential stress acting on the interface between the inner matrix and substrate

(reinforcement, matrix and masonry) but also by the configuration of the reinforcement (generally composed by a grid) and the possible damage of the matrix. In this regard, some studies ([15,22]) underlined the main differences of the bond behavior of FRCM systems with respect to composite systems made of organic matrices (Fiber Reinforced Polymer systems, FRP).

The complexity of the local failure phenomena occurring inside an FRCM reinforcing package and the boundary conditions to apply in the different cases of practical interest (namely entire reinforced structures or real scale structural elements) cannot leave aside the utilization of computerized methods, which are often (albeit not always) based on a classic FE discretization. It is in fact notorious that the most diffused and straightforward approach available in the literature to deal with such kind of problems relies into the direct utilization of Finite Elements with softening materials. Both standard and non-standard numerical procedures have been already presented in the specialized literature.

For instance, a standard approach which is quite common relies into the heterogeneous discretization of matrix and fiber layers, joined together by means of softening interfaces [31,32]. Typically, conventional non-linear FE material models (such as the Concrete Damage Plasticity CDP model in Abaqus, coupled with cohesive interfaces) are used. Unfortunately, the computational burden is quite high even for the analysis of small laboratory samples. Furthermore, from a theoretic point of view, the procedures proposed merely consist of a special application of consolidated typologies of material models in a specific field of research. Premature halting and a dependence of the results on the many input parameters to set for the materials represent classic sources of difficulties that a standard user is asked to face with.

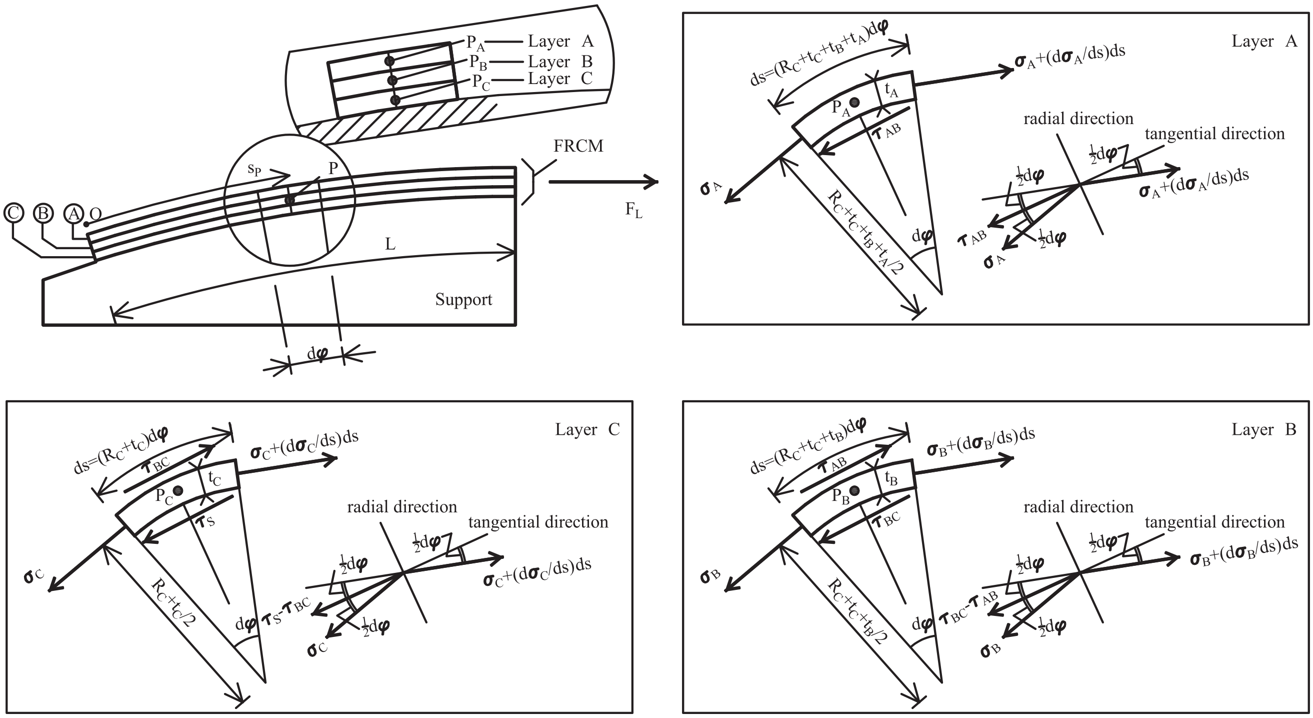

Fig. 1. Mechanical model adopted for an FRCM applied to an infinitely stiff curved substrate.

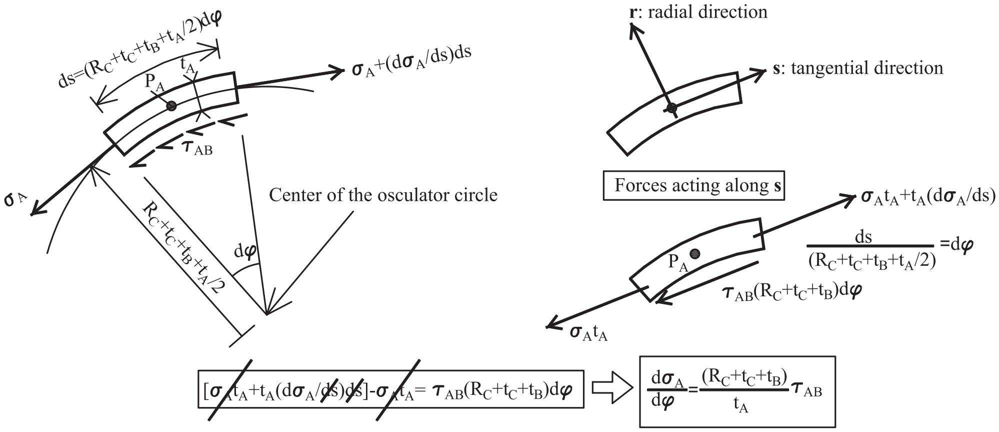

Fig. 2. Derivation of the longitudinal equilibrium equation for Layer A, curved FRCM reinforcement.

Other procedures include, for instance, the specialization of the general method known as phase field theory [33–37], *peri*-dynamics [38], high order beam theory [39,40], etc.

For instance, Donnini and co-workers in [37] specialized the model proposed by Alessi and Freddi [36] for hybrid laminates, revising and adapting it to the specific problem of FRCM coupons. In particular, they schematized the coupons as multilayer systems constituted by mortar, reinforcement and interfaces. Each layer was modeled as a brittle bar subjected to tensile stress, with energy stored constituted by three contributions, as usual in phase field theories, namely an elastic part, a local damage term and a non-local gradient part.

In any case, all the aforementioned numerical procedures require in the majority of the cases sophisticated numerical tools integrated in existing advanced FE codes and experienced users with a strong theoretical background in the field. For a common user, such features represent an issue if the aim is the application of the models to the preliminary design phase of a reinforcement for real scale masonry structures to upgrade.

Despite the interest towards the use of FRCM systems and the applications on curved structures, only in recent years studies concerning the bond behavior of FRCM systems externally applied to curved masonry substrates have been carried out ([32–50]). In particular, while some of these studies analyzed this topic from an experimental point of view ([32–45]), the others proposed different theoretical/analytical approaches for studying the local bond behavior of FRCM systems applied to curved masonry substrates ([44–50]). Among these, the Authors recently proposed numerical modeling approaches based on both a simplified schematization of the reinforcing system by means of spring elements [47] and a more advanced schematization based on a heterogeneous Finite Element micro modelling [48]. Both the approaches showed a good reliability in reproducing the experimental tests and, at the same time, they allowed for analyzing the role of key parameters such as the curvature and the position of the reinforcement (at the intrados or extrados) on the bond behavior.

However, they are affected by the limitation that their applicability is strictly limited to small samples under the imposition of simple

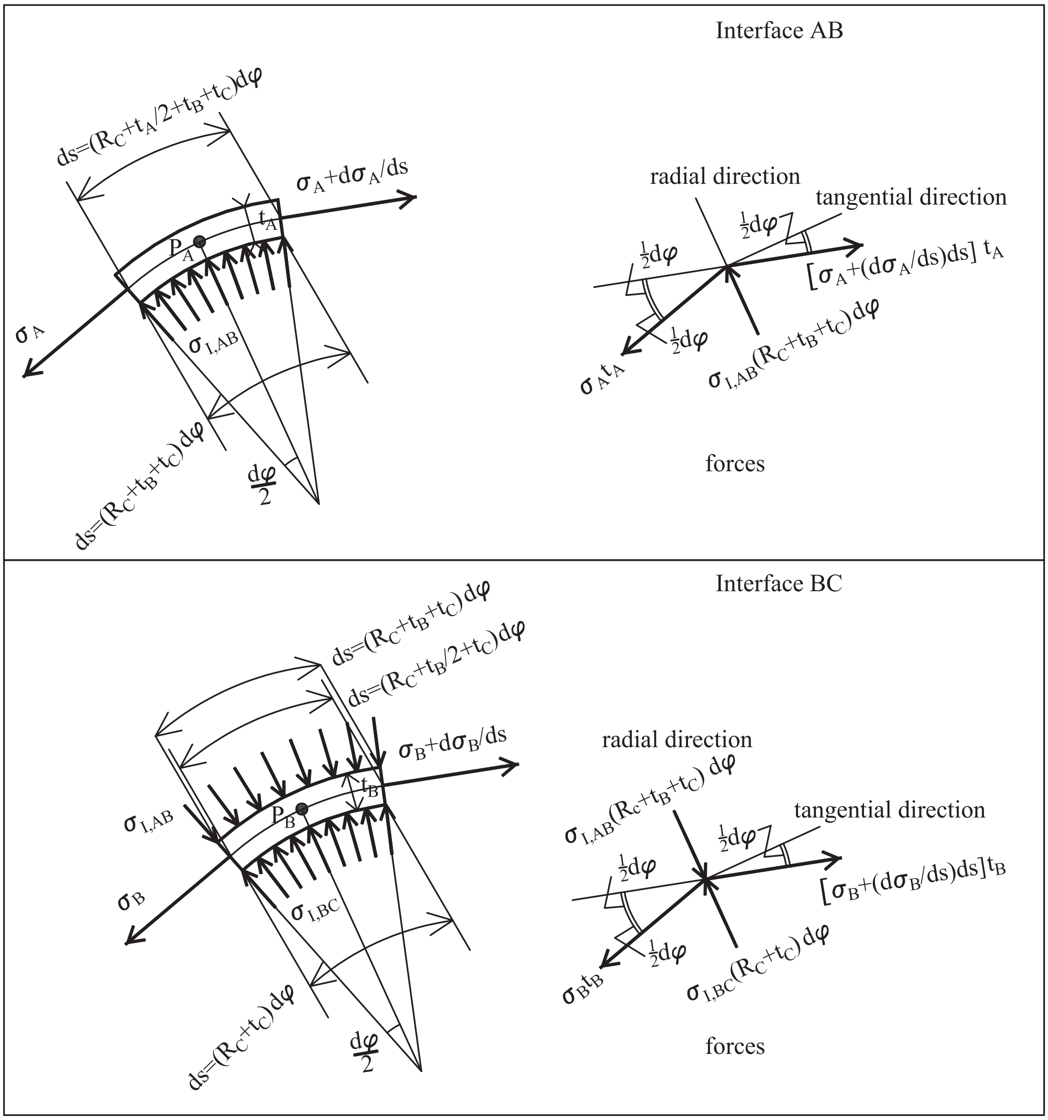

Fig. 3. Forces acting on layers A & B to evaluate normal stresses acting on interfaces AB and BC by imposing the equilibrium along the radial direction.

boundary conditions.

The present approach leaves aside Finite Elements FEs and therefore allows to repeat rapidly debonding sensitivity analyses, which in turn permits to easily calibrate a simplified constitutive behavior for the reinforcement package, considered globally. Such approach appears particularly suitable in its utilization in a second phase, i.e. in Finite Element computations of entire masonry arches and vaults reinforced with FRCM. In the preparation phase for large scale structural applications, the advantage is evident. The aim is indeed to model the reinforcement with truss elements perfectly bonded to the substrate and exhibiting an elasto-damaging behavior in tension [51,52], truly equivalent to the FRCM composite package, but much more manageable. It is expected that the stability of the non-linear numerical analyses is boosted considerably, at the same time giving the possibility to retain the actual behavior of FRCM in terms of debonding from the substrate, at least globally.

In particular, a semi-analytical approach for the study of the debonding mechanism of FRCM systems externally applied at the intrados or extrados of curved masonry pillars is presented. The main feature of the approach consists of modeling the FRCM reinforcing system in three separated components, external mortar layer, central fiber net and internal mortar layer, assumed subjected to a longitudinal state of stress and interacting among them by means of interfacial tangential stresses. The reinforcement, assumed applied to a curved rigid and infinitely resistant substrate, is able to transfer the force applied at its loaded end by means of an elastic interface interposed between the substrate and the internal mortar layer. Particular regard is devoted to the schematization of the constitutive behavior of the interfaces interposed between the reinforcement and the two mortar layers: a trilinear relationship between tangential stress and slip is indeed assumed, in order to capture the initial undamaged phase, the post-peak strength degradation phase (softening) and the residual strength phase, according to the experimental evidence [43]. Since in case of curved substrates, by equilibrium, normal stresses at the interfaces between fiber and matrix arise, such feature is suitably taken into account in the model modifying the peak tangential resistance and the ductility through a classic Mohr-Coulomb criterion.

From a mathematical point of view, the three longitudinal equilibrium equations written for fiber (Layer B), outer and inner mortar layers (A & C) can be suitably manipulated in such a way that the field problem to solve is constituted by a system of first order differential equations where the independent variables are the longitudinal stresses of the three layers and their longitudinal displacements. Normal stresses acting at the interface between fiber and inner/outer mortar are deduced by

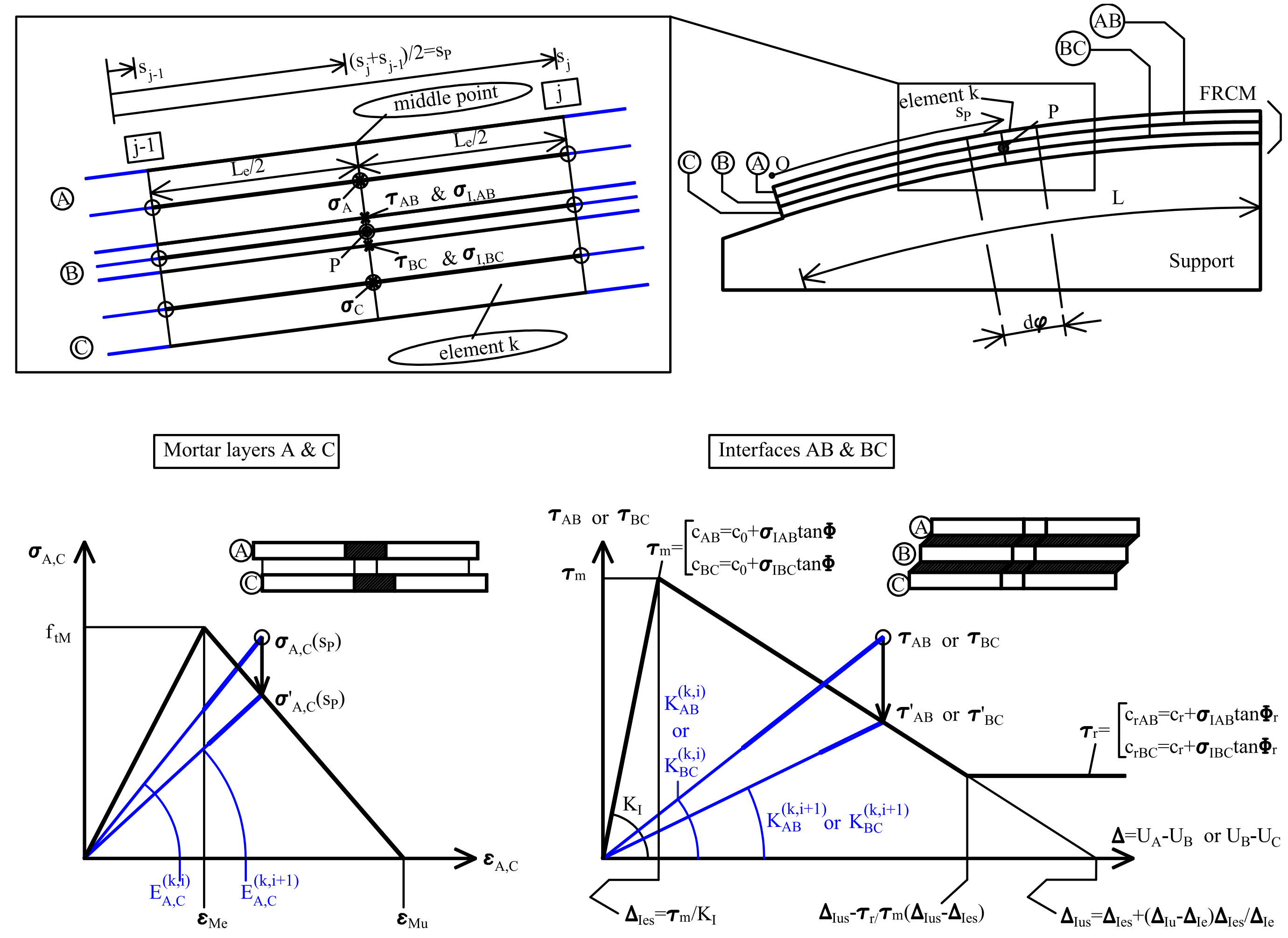

Fig. 4. Updating strategy of the elastic properties for an element k at the end of the *i*-th load step, mortar layers A & C and interfaces AB & BC.

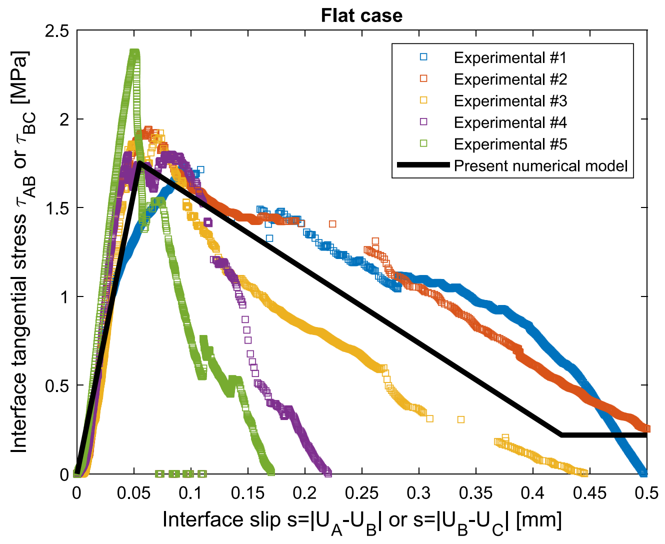

Fig. 5. Comparison between the adopted fiber-mortar interface constitutive behavior and experimental data obtained on the same FRCM package applied on a flat masonry substrate.

Table 1
Shear tests carried out at the University of Florence. Mechanical and geometrical properties adopted for the different components.

Quantity	Symbol	Value	Unit of measure
Dry fiber elastic modulus	E_B	241	GPa
Equivalent thickness of the warp mesh (layer B thickness)	t_B	0.045	mm
Layer A & C elastic modulus	$E_A = E_C$	5000	MPa
Thickness of the mortar layers	$t_A = t_C$	4	mm
Layer A & C tensile strength	f_{tM}	5.05	MPa
Layer A & C strain at the elastic limit	ε_{Me}	f_{tM}/E_A	–
Layer A & C ultimate tensile strain	ε_{Mu}	$2\,\varepsilon_{Me}$	–
Matrix-fiber interface slip at the elastic limit	Δ_{Ie}	0.055	mm
Matrix-fiber interface ultimate slip	Δ_{Iu}	$0.425 + \frac{3000}{R_c}\Delta_{Ie}$	mm
Cohesion of the intact interface	c_0	1.75	MPa
Interface residual cohesion	c_r	$1/8\ c_0$	MPa
Initial interface friction angle	Φ	40°	Deg
Residual friction angle	Φ_r	25°	Deg
Elastic stiffness interface S	K_S	$10c_0/\Delta_{Ie}$	N/mm^3

radial equilibrium; their presence modifies the ductility and strength of the interfaces, with intuitive beneficial effect for an extrados reinforcement and detrimental for an intrados one. If all the materials behave elastically, a closed form solution can be easily derived.

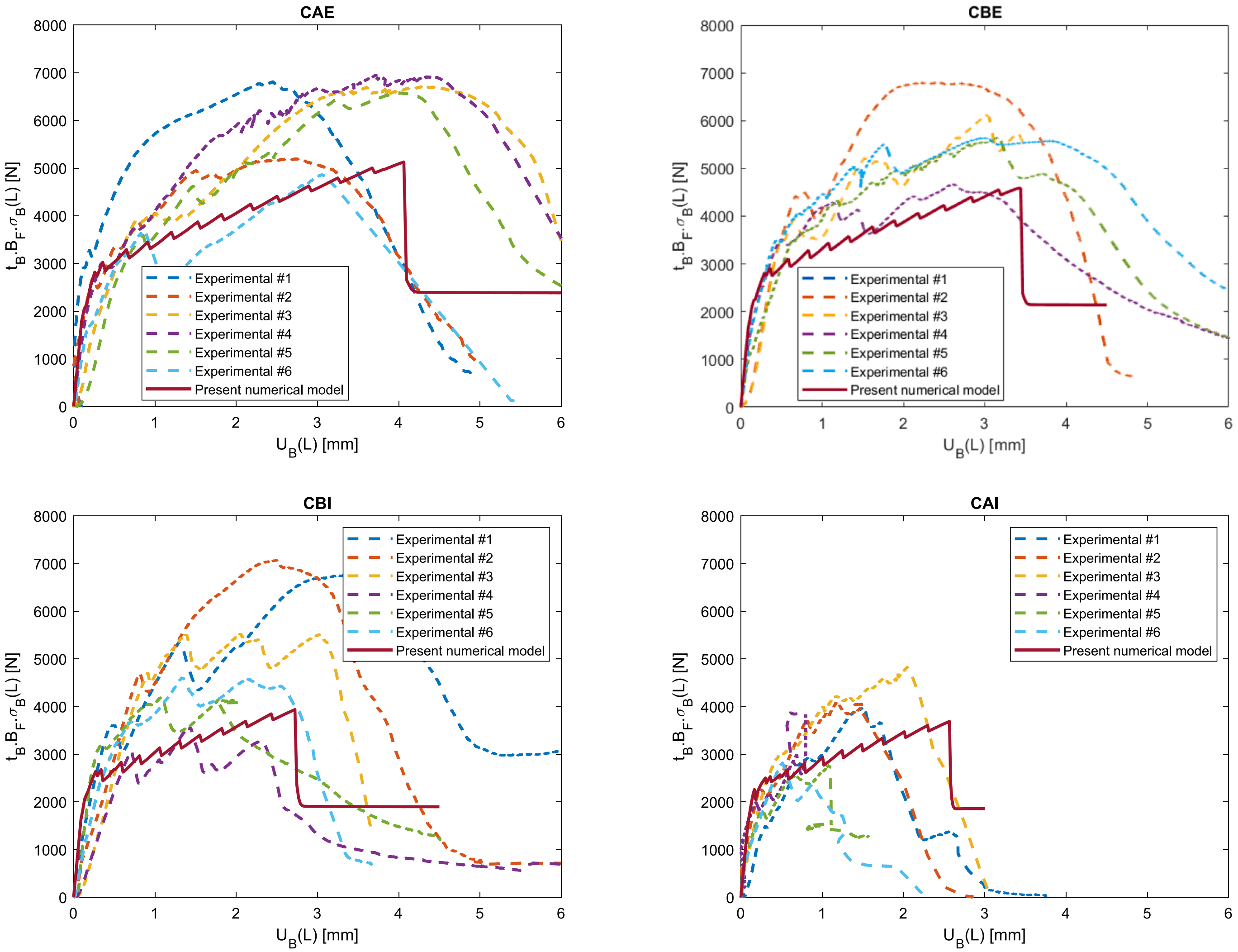

Fig. 6. Global behavior of CAE, CBE, CBI, CAI specimens (in clockwise direction from the top-left subfigure). Comparison between present model results and experimental data.

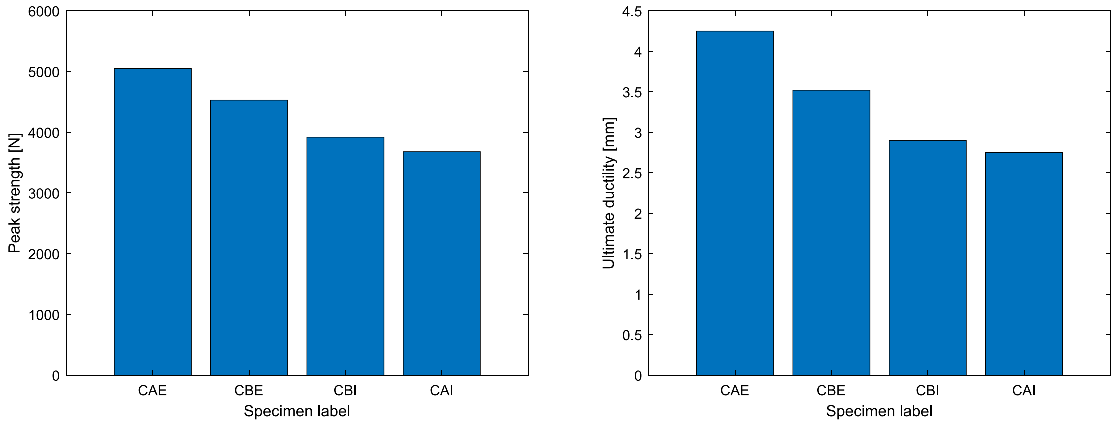

Fig. 7. Numerical peak strength (-a) and ultimate displacement (-b) obtained for CAE, CBE, CBI and CAI.

Consequently, a fully explicit iterative algorithm to deal with non-linearities is proposed that bases on dealing with elastic materials at each load step. It relies into the progressive relaxation of the stiffness when the softening branch is activated in one of the components of the reinforcing system, following an idea already proposed in [53–55]. Its main futures are represented by the great robustness and the need to solve iteratively only elastic problems with progressively reduced stiffness of the elements.

Whilst there are some formal similarities in the physical model with the phase field method, the incremental procedure used here is fully

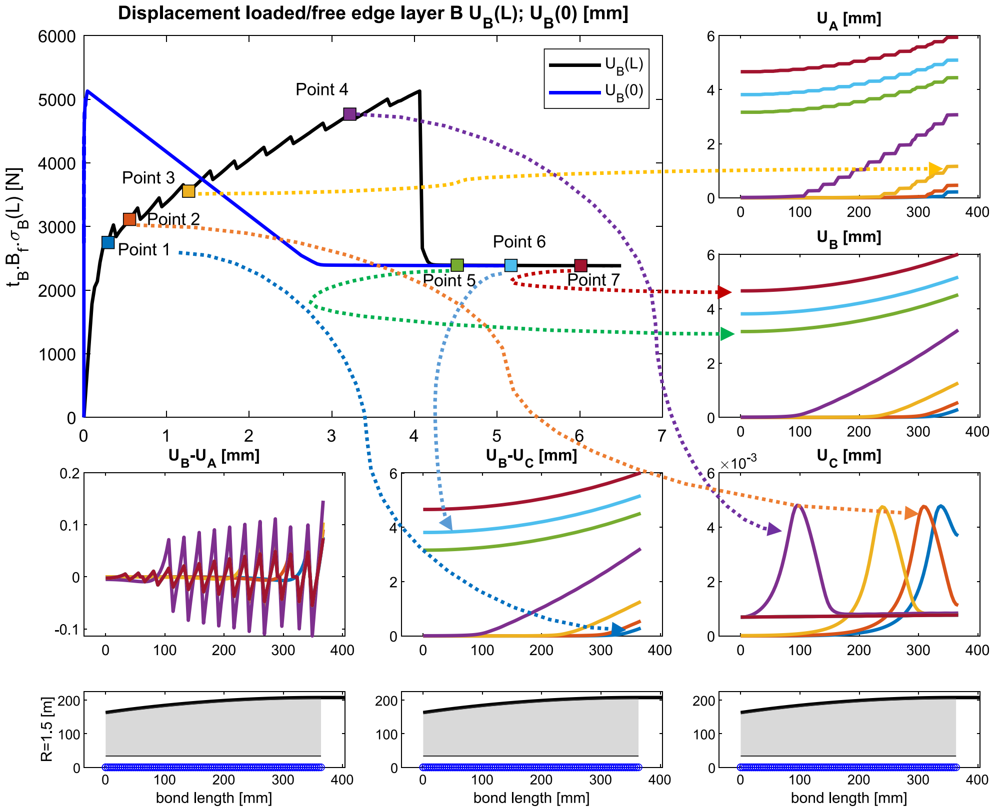

Fig. 8. CAE data. From the top-left in clockwise order. Force $t_B B_f \sigma_B(L)$ - displacement $U_B(L)$, $U_B(0)$ curves; U_A, U_B, U_C, $U_B - U_C$, $U_B - U_A$ behavior along the bond length (the color of the curves corresponds to the particular instants investigated during the loading process and matches that of the points represented in the top-left sub-figure).

explicit and much easier. The major advantage relies indeed into dealing with an elastic problem at each time step, where the structure is constituted by many small trusses positioned in parallel that interact with elastic interfaces mutually exchanging tangential stresses. There are therefore, by definition, no numerical issues possible because the problem is well posed, and the solution found is characterized by the uniqueness property typical of the elastic materials. In general, the algorithms adopted in other models available in the literature are much more complex, for instance in [37] the evolution problem is formulated as a constrained quadratic programming solved at each load increment. Consequently, also the numerical efficiency is in favor of the present approach, because only a factorization of a medium scale elastic matrix is needed at each time step.

The semi-analytical approach can be applied for any problem of FRCM debonding in presence of concrete and masonry, possibly curved, substrates and -thanks to its robustness, simplicity and the reduced time needed for obtaining the results-, may represent a valuable tool in the preliminary design of FRCM strengthening systems. The capability of the proposed modeling approach to capture the experimental bond behavior is assessed in the paper with reference to experimental tests carried out by the Authors and presented in [43].

2. Mathematical model in case of curved substrates

Let us consider a curved substrate reinforced with FRCM and subjected to a standard shear-lap test, see Fig. 1.

For the reinforcing pack, three layers are considered, namely the outer and inner matrix (layers A and C) and the central fiber (layer B) embedded between A & C. The following hypotheses are done: (i) all layers are assumed in a monoaxial stress state acting longitudinally; (ii) layers A & C are characterized by a constitutive behavior that is non-linear with softening in tension, layer B is linear elastic; (iii) all layers are assumed interacting by means of possibly non-linear interfaces. The reinforcing pack is then assumed connected to a rigid infinitely resistant substrate. An elastic interface is interposed between them, to account for the actual deformability of the substrate (if not negligible).

The kinematic variables are the longitudinal displacements of the three layers, labeled from the extrados to the intrados with U_A, U_B and U_C respectively. Let indicate with L the bonded length, with R_C the curvature radius of the interface and with t_A, t_B and t_C the thickness of layers A, B, C, respectively. The out-of-plane width is assumed unitary. As far as the static variables are concerned, let indicate with σ_A, σ_B and σ_C the longitudinal stresses acting on the three layers, listed in order from the outer to the inner one. At the interface A-B between layers A and B, a tangential stress τ_{AB} is exchanged; similarly, τ_{BC} acts at the interface between layers B and C. Finally, τ_S acts at the interface between inner matrix and substrate. Due to the curvature of the substrate, by equilibrium, at the interfaces A-B and B-C normal stresses arise, which are respectively denoted with $\sigma_{I,AB}$ and $\sigma_{I,BC}$.

For illustrative purposes, let us isolate an infinitesimal portion of Layer A, $\left(R_C + t_C + t_B + \frac{t_A}{2}\right)d\varphi$ long, as illustrated in detail in Fig. 2.

Similar considerations can be repeated for Layers B & C, with no conceptual differences in the derivation of the field equations. For the sake of conciseness, no further details are given to the reader. Here it is only emphasized that, isolating an infinitesimal longitudinal portion of the reinforcing pack identified by $d\varphi$ and hereafter called (k), see Fig. 1, the following three equilibrium equations along the longitudinal direction, each referring to one of the three layers, can be written:

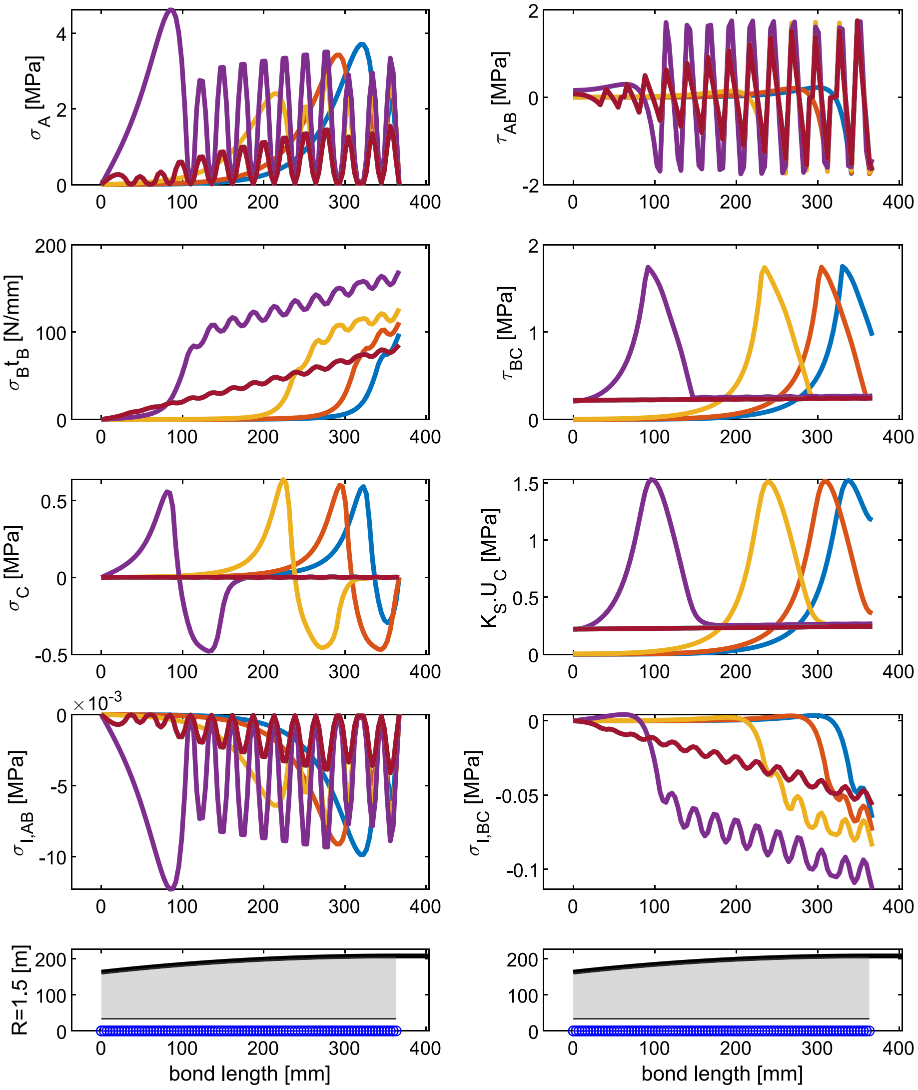

Fig. 9. CAE data. From the top-left in clockwise order. σ_A, τ_{AB}, τ_{BC}, $K_S U_C$, $\sigma_{I,BC}$, $\sigma_{I,AB}$, σ_C, $\sigma_B t_B$ behavior along the bond length (the color of the curves corresponds to the particular instants investigated during the loading process and matches that of the points represented in the previous sub-figure).

$$
\begin{aligned}
\frac{d\sigma_A}{d\varphi} &= \frac{R_C + t_B + t_C}{t_A}\tau_{AB} \\
\frac{d\sigma_B}{d\varphi} &= \frac{R_C + t_C}{t_B}\tau_{BC} - \frac{R_C + t_B + t_C}{t_B}\tau_{AB} \\
\frac{d\sigma_C}{d\varphi} &= \frac{R_C}{t_C}\tau_S - \frac{R_C + t_C}{t_C}\tau_{BC}
\end{aligned}
\tag{1}
$$

Let us assume that the non-linear problem is solved at each load step by means of a strategy of reduction of the elastic modulus/stiffness of that component of the reinforcement (matrix and interfaces) exceeding the elastic limit in the previous load step. Let assume, at a certain load step (i) and for a certain infinitesimal portion (k) of the reinforcement, that the elastic moduli of layers A, B and C are respectively equal to $E_A^{(i,k)}$, $E_B^{(i,k)}$ and $E_C^{(i,k)}$. The same hypotheses hold for the elastic stiffnesses of the interfaces AB, BC and S, labeled respectively with symbols $K_{AB}^{(i,k)}$, $K_{BC}^{(i,k)}$ and $K_S^{(i,k)}$.

Under such assumptions, Eq. (1) can be re-written as follows:

$$
\begin{aligned}
\sigma_A &= \frac{E_A^{(i,k)}}{R_C + \frac{t_A}{2} + t_B + t_C}\frac{dU_A}{d\varphi} \\
\sigma_B &= \frac{E_B^{(i,k)}}{R_C + \frac{t_B}{2} + t_C}\frac{dU_B}{d\varphi} \\
\sigma_C &= \frac{E_C^{(i,k)}}{R_C + \frac{t_C}{2}}\frac{dU_C}{d\varphi} \\
\frac{d\sigma_A}{d\varphi} &= \frac{R_C + t_B + t_C}{t_A}K_{AB}^{(i,k)}(U_A - U_B) \\
\frac{d\sigma_B}{d\varphi} &= \frac{R_C + t_C}{t_B}K_{BC}^{(i,k)}(U_B - U_C) - \frac{R_C + t_B + t_C}{t_B}K_{AB}^{(i,k)}(U_A - U_B) \\
\frac{d\sigma_C}{d\varphi} &= \frac{R_C}{t_C}K_S^{(i,k)}U_C - \frac{R_C + t_C}{t_C}K_{BC}^{(i,k)}(U_B - U_C)
\end{aligned}
\tag{2}
$$

It should be noted that in Eq. (2) the first three equations represent the elastic constitutive behavior of layers A, B and C, bearing in mind that $E_B^{(i,k)}$ and $K_S^{(i,k)}$ remain unaltered in the subsequent loading steps, because the materials are assumed infinitely elastic.

Eq. (2) can be rearranged in the following matrix form:

$$
\begin{aligned}
&\frac{d\mathbf{Y}^{(i,k)}}{d\varphi} = \mathbf{K}^{(i,k)}\mathbf{Y} = \begin{bmatrix} \mathbf{O}_{3x3} & \mathbf{K}_1^{(i,k)} \\ \mathbf{K}_2^{(i,k)} & \mathbf{O}_{3x3} \end{bmatrix} \mathbf{Y}^{(i,k)} \\
&\frac{d\mathbf{Y}^{(i,k)}}{d\varphi} = \begin{bmatrix} \frac{dU_A^{(i,k)}}{d\varphi} & \frac{dU_B^{(i,k)}}{d\varphi} & \frac{dU_C^{(i,k)}}{d\varphi} & \frac{d\sigma_A^{(i,k)}}{d\varphi} & \frac{d\sigma_B^{(i,k)}}{d\varphi} & \frac{d\sigma_C^{(i,k)}}{d\varphi} \end{bmatrix}^T \\
&\mathbf{Y}^{(i,k)} = [\, U_A \quad U_B \quad U_C \quad \sigma_A \quad \sigma_B \quad \sigma_C \,]^T \\
&\mathbf{K}_1^{(i,k)} = \begin{bmatrix} \frac{R_C + \frac{t_A}{2} + t_B + t_C}{E_A^{(i,k)}} & 0 & 0 \\ 0 & \frac{R_C + \frac{t_B}{2} + t_C}{E_B^{(i,k)}} & 0 \\ 0 & 0 & \frac{R_C + \frac{t_C}{2}}{E_C^{(i,k)}} \end{bmatrix} \\
&\mathbf{K}_2^{(i,k)} = \begin{bmatrix} \frac{R_C + t_B + t_C}{t_A} K_{AB}^{(i,k)} & -\frac{R_C + t_B + t_C}{t_A} K_{AB}^{(i,k)} & 0 \\ -\frac{R_C + t_B + t_C}{t_B} K_{AB}^{(i,k)} & \frac{R_C + t_C}{t_B} K_{BC}^{(i,k)} + \frac{R_C + t_B + t_C}{t_B} K_{AB}^{(i,k)} & -\frac{R_C + t_C}{t_B} K_{BC}^{(i,k)} \\ 0 & -\frac{R_C + t_C}{t_C} K_{BC}^{(i,k)} & \frac{R_C + t_C}{t_C} K_{BC}^{(i,k)} + \frac{R_C}{t_C} K_S^{(i,k)} \end{bmatrix} \\
&\mathbf{O}_{3x3} = \begin{bmatrix} 0 & 0 \\ 0 & 0 \end{bmatrix}
\end{aligned}
\tag{3}
$$

where the superscript (i,k) indicates any quantity pertaining to the position (k) at the (i)-th load step. Eq. (3) is a first order ODE system whose solution can be found analytically evaluating the eigenvectors and eigenvalues of $\mathbf{K}^{(i,k)}$.

The solution of the field problem for a single element (k) at the (i)-th load step is the following:

$$
\begin{aligned}
\mathbf{Y}^{i,k}\left(C_q^{i,k}, \varphi\right) = {} & C_1^{i,k}\mathbf{E}_{V1}^{i,k} e^{\lambda_1^{i,k}\varphi} + C_2^{i,k}\mathbf{E}_{V2}^{i,k} e^{\lambda_2^{i,k}\varphi} + C_3^{i,k}\mathbf{E}_{V3}^{i,k} e^{\lambda_3^{i,k}\varphi} \\
& + C_4^{i,k}\mathbf{E}_{V4}^{i,k} e^{\lambda_4^{i,k}\varphi} + C_5^{i,k}\mathbf{E}_{V5}^{i,k} e^{\lambda_5^{i,k}\varphi} + C_6^{i,k}\mathbf{E}_{V6}^{i,k} e^{\lambda_6^{i,k}\varphi}
\end{aligned}
\tag{4}
$$

where the symbols have the following meaning:

- $C_q^{i,k}$ is an integration constant $q = 1, \cdots, 6$;
- $\mathbf{Y}^{i,k}$ is the solution vector;
- $\mathbf{E}_{Vq}^{i,k}$ and $\lambda_q^{i,k}$ are respectively the eigenvectors and the eigenvalues pertaining to element k at the load step i.

For all elements, except the first and last ones located at the free and loaded edges, the continuity of the stresses and displacements between elements $k-1/k$ should be imposed. Therefore, the following 6 equations are written in the 12 unknowns $C_q^{i,k}$ and $C_q^{i,k-1}$:

$$
-\mathbf{Y}^{i,k}\left(C_q^{i,k-1}, \varphi_j\right) + \mathbf{Y}^{i,k}\left(C_q^{i,k}, \varphi_j\right) = 0_{6\times1}
\tag{5}
$$

where the symbols have the following meaning:

- $0_{6\times1}$ is a 6 × 1 vector of all zeros;
- φ_j identifies the interface section between elements $k-1/k$.

Eq. (5) should be written for all internal interfaces between contiguous elements, so assuming to subdivide the entire bond length into n_e small portions, $6n_e - 6$ equalities are derived.

For the free edge node, the following 3 equations are written, imposing that the normal stress on the three layers A-C is equal to zero:

$$
\mathrm{diag}(\,0 \quad 0 \quad 0 \quad 1 \quad 1 \quad 1\,)\mathbf{Y}^{i,1}\left(C_q^{i,1}, 0\right) = 0_{6\times1}
\tag{6}
$$

For the loaded edge, other three equations are written:

$$
\begin{aligned}
&\mathrm{diag}(\,0 \quad 1 \quad 0 \quad 1 \quad 0 \quad 1\,)\mathbf{Y}^{i,n_e}\left(C_q^{i,n_e}, \varphi_L\right) = \left[\,0 \quad U_{BL}^{i,n_e} \quad 0 \quad 0 \quad 0 \quad 0\,\right]^T \\
&\quad = \mathbf{U}_{BL}^{i,n_e}
\end{aligned}
\tag{7}
$$

where U_{BL}^{i,n_e} is the displacement applied on the loaded edge of layer B at the time step i and φ_L is defined as follows:

$$
\varphi_L = \frac{L}{R_C + t_A + t_B + t_C}
\tag{8}
$$

Leaving out in Eqs. (6) and (7) the identity equations and considering Eqs. (5), (6) and (7) contemporarily, they constitute a linear system of $6n_e$ equations into $6n_e$ unknowns, the latter being the $C_q^{i,k}$ (from $k = 1$, first element located at the free edge to $k = n_e$, last element at the loaded edge) integration constants of all the elements.

Suitably assembling the previously introduced equations, the problem is reformulated as follows:

$$
\mathbf{C}^i\mathbf{K}^i = \mathbf{U}_{BL}^i
\tag{9}
$$

where $\mathbf{C}^i$, $\mathbf{K}^i$ and $\mathbf{U}_{BL}^i$ are respectively the assembled vector of the integration constants of all the elements, the assembled square matrix of the coefficients of Eqs. (5), (6) and (7) and the vector of external loads applied at the time step i. $\mathbf{U}_{BL}^i$ is a vector of all zeros, exception made for

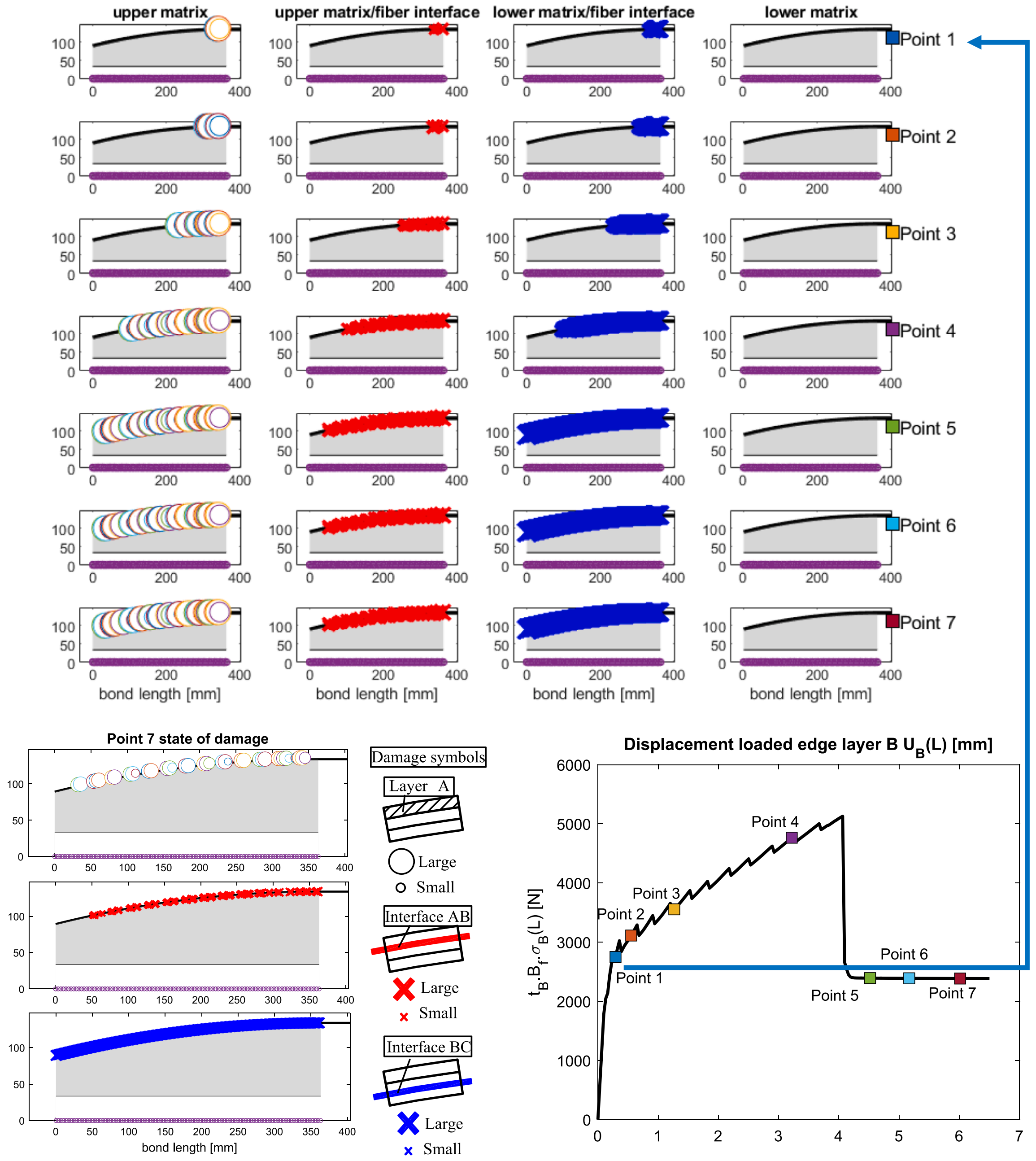

Fig. 10. CAE data. Propagation of damage inside mortar layers and interfaces at the different instants investigated during the loading process. White circles and red/blue crosses represent mortar and interface damage, respectively. Their dimension is proportional to the amount of damage. (For interpretation of the references to color in this figure legend, the reader is referred to the web version of this article.)

the third last component which is equal to the displacement U_{BL}^{i,n_e}, imposed at the loaded edge on layer B.

It is also interesting to point out that different boundary conditions can be also written, for instance an applied displacement at the free edge of layer B, $U_{B0}^{1,k}$. In such a case, Eqs. (6) and (7) rewrite as follows:

$$\begin{aligned}&\mathrm{diag}(0\quad 1\quad 0\quad 1\quad 1\quad 1)\mathbf{Y}^{1,k}\left(C_q^{1,k},0\right)=\begin{bmatrix}0 & U_{BL}^{1,k} & 0 & 0 & 0 & 0\end{bmatrix}^T\\&\mathrm{diag}(0\quad 0\quad 0\quad 1\quad 0\quad 1)\mathbf{Y}^{2n_e-1,k}\left(C_q^{2n_e-1,k},L\right)=0_{6\times 1}\end{aligned} \tag{10}$$

By means of the imposition of the BCs written in Eq. (10), it is possible to simulate the snap back observed after the attainment of the peak load, which is documented in the literature [17–19].

By inversion of matrix $\mathbf{K}^k$, $\mathbf{C}^k$ vector is computed through Eq. (9) and finally $\mathbf{Y}^{j,k}$ is derived for each element k via Eq. (5).

In order to find $\sigma_{I,AB}$ and $\sigma_{I,BC}$, it is necessary to wimpose equilibrium for two infinitesimal portions with amplitude $d\varphi$ of layers A and A + B, as illustrated in Fig. 3:

$$\begin{aligned}\sigma_{I,AB}&=\frac{\sigma_A t_A}{R_C+t_B+t_C}\\\sigma_{I,BC}&=\frac{\sigma_B t_B}{R_C+t_C}-\frac{R_C+t_B+t_C}{R_C+t_C}\sigma_{I,AB}\end{aligned} \tag{11}$$

From the previous equation, it is interesting to notice that $\sigma_{I,AB}$ and $\sigma_{I,BC}$ can be found at the end of each load step knowing σ_A and σ_B. $\sigma_{I,AB}$ and $\sigma_{I,BC}$ are then used to modify in the new load step the constitutive law of the interfaces, as it will be explained in detail in the following sub-sec-

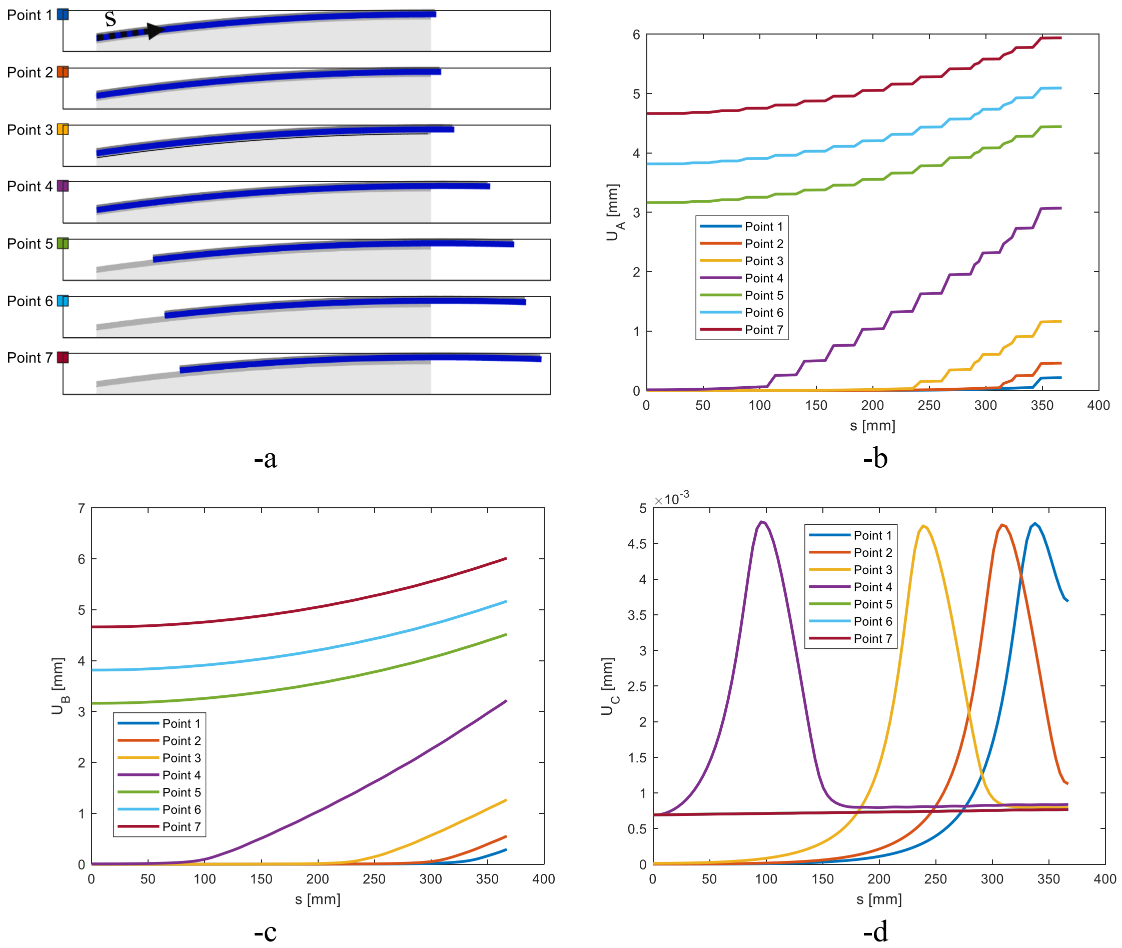

Fig. 11. CAE data. Deformed shapes of the reinforcement package (-a) at 7 values of the displacement $U_B(L)$ applied at the loaded edge. -b: $U_A(s)$ (displacement of the outer matrix layer). -c: $U_B(s)$ (displacement of the fiber). -d: $U_C(s)$ (displacement of the inner matrix layer).

tion.

2.1. Stiffness update for non-linear materials

The non-linearity is tackled by means of a sequence of linear problems, in agreement with the strategy proposed recently in [53–55], where the softening behavior is approximated by means of a sawtooth constitutive law. The idea is particularly simple and robust and allows to deal with strong non-linearities of the material by means of a sequence of elastic analyses.

The behavior of mortar layers A & C and interfaces AB & BC is assumed in this paper trilinear, as illustrated in Fig. 4.

In particular, for mortar layers, softening is assumed only in tension, whereas the compressive behavior is indefinitely elastic. The stress–-strain curve is defined by the strain at the elastic limit ε_{Me}, the tensile strength f_{tM} and the ultimate strain ε_{Mu}.

Considering only layer A (the procedure is identical for layer C) and focusing on a single element k, at the end of step i, if $\sigma_A > f_{tM}$, the normal stress is projected on the softening curve as follows:

$$\sigma'_A = \max\left\{\frac{\varepsilon_{Mu} - \frac{\sigma_A}{E_A^{(k,i)}}}{\varepsilon_{Mu} - \varepsilon_{Me}} f_{tM}; 0\right\} \tag{12}$$

and the updated Young's modulus is:

$$E_A^{(k,i+1)} = \frac{\sigma'_A}{\sigma_A} E_A^{(k,i)} \tag{13}$$

σ_A is the longitudinal stress of layer A calculated at the middle point of element k, as detailed in Fig. 4. If the elements are sufficiently short, such simplification does not have perceivable consequences of the accuracy of the results obtained.

For the interfaces AB & BC, the trilinear behavior is defined by the slip at the elastic limit Δ_{Ie}, the ultimate slip Δ_{Iu}, the cohesion of the intact interface c_0, the residual cohesion c_r, the initial friction angle Φ and the residual friction angle Φ_r. A Mohr-Coulomb law is assumed to update both the peak and the residual strength in presence of normal stresses different from zero. The ultimate slip changes accordingly, as it is detailed hereafter.

Considering again only the interface AB for the sake of brevity, then $\sigma_{I,AB}$ is known everywhere along the length L_e of the element, in agreement with Eq. (11). In the same way adopted for layer A, the algorithm modifies the stiffness of the interface for the element k, checking the stress state of the interface in the middle of the element.

Denoting with $\sigma_{I,AB} = \sigma_{I,AB}(s_P)$ the normal stress at the middle point at the end of the load step i, the constitutive law of the interface is modified as follows (the reader is referred to Fig. 4 for the meaning of the symbols):

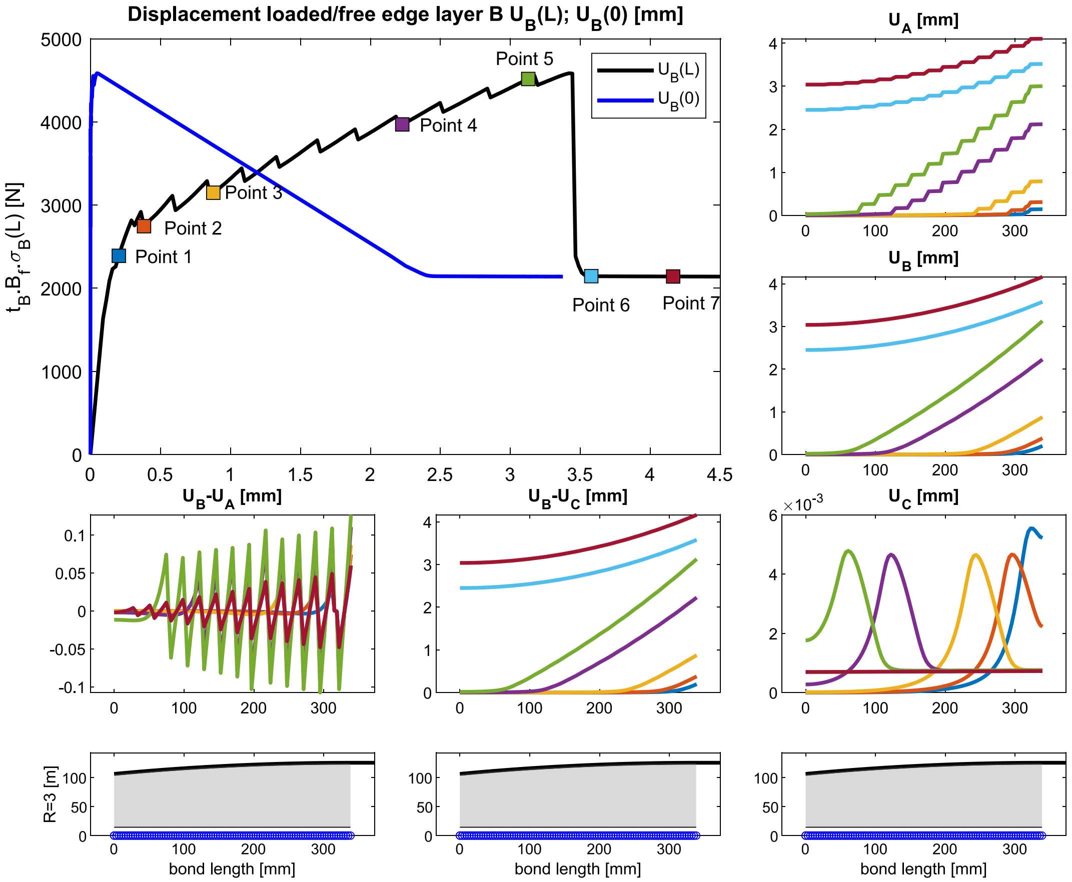

Fig. 12. CBE data. From the top-left in clockwise order. Force $t_B B_f \sigma_B(L)$ - displacement $U_B(L)$, $U_B(0)$ curves; U_A, U_B, U_C, $U_B - U_C$, $U_B - U_A$ behavior along the bond length (the color of the curves corresponds to the particular instants investigated during the loading process and matches that of the points represented in the top-left sub-figure).

$$\begin{aligned}
\tau_m &= c_0 + \sigma_{I,AB}\tan(\Phi) \\
\tau_r &= c_r + \sigma_{I,AB}\tan(\Phi_r) \\
K_I &= \frac{c_0}{\Delta_{Ie}} \\
\Delta_{Ies} &= \frac{\tau_m}{K_I} \\
\Delta_{Ius} &= \Delta_{Ies} + (\Delta_{Iu} - \Delta_{Ie})\frac{\Delta_{Ies}}{\Delta_{Ie}}
\end{aligned} \tag{14}$$

In case that τ_{AB} at the end of step i exceeds τ_m, the tangential stress is projected on the softening curve as follows:

$$\tau'_{AB} = \frac{\Delta_{Ius} - \frac{\tau_{AB}}{K_{AB}^{(k,i)}}}{\Delta_{Ius} - \Delta_{Ies}}\tau_m \tag{15}$$

The updated interface stiffness to use in the new iteration is the following:

$$K_{AB}^{(k,i+1)} = \frac{\tau'_{AB}}{\tau_{AB}} K_{AB}^{(k,i)} \tag{16}$$

If $\frac{\tau_{AB}}{K_{AB}^{(k,i)}} > \Delta_{Ius} - \frac{\tau_r}{\tau_m}(\Delta_{Ius} - \Delta_{Ies})$, the stress is projected on the horizontal plateau, so that the updated stiffness for the new iteration is the following:

$$K_{AB}^{(k,i+1)} = \frac{\tau_r}{\tau_{AB}} K_{AB}^{(k,i)} \tag{17}$$

3. Numerical analyses

The quasi-analytical approach here proposed is tested in its reliability considering a comprehensive experimental campaign (shear-lap tests) carried out by the authors in [43] on 4 different sets of curved masonry pillars reinforced with FRCM.

The specimens are small masonry columns constituted by 5 common Italian clay bricks (dimensions: 250x120x65 mm) interspersed with 4 thick mortar joints (thickness: 10–23 mm) and disposed one over the other in a slight bent. The intent was to study the performance of an FRCM reinforcement in case of application to arches.

The four sets are labeled respectively with CAE, CBE, CBI and CAI. CAE and CBE are the specimens with extrados reinforcements, whereas in CBI and CAI, the FRCM strip is applied at the intrados. CAE and CBE (or analogously CAI and CBI) differ only for the curvature radii of the surface where the reinforcement is applied, respectively equal to 1500 and 3000 mm. The experimental results, in terms of global applied force-slip at the loaded edge curves, are at disposal in the same reference paper [43] for six replicates per set.

The FRCM strengthening system is constituted by two layers (A & C) 4 mm thick of mortar catalogued as M20 according to the Italian standard and by a central layer B relying into a bi-directional 70 + 18 g/m^2 PBO mesh (70 g/m^2 in the warp direction and 18 g/m^2 in the weft direction). The authors have already provided a comprehensive experimental characterization of all the materials constituting the FRCM, also providing the interface between mortar and PBO mesh constitutive behavior, see Fig. 5. and [42]. Such information was retrieved by means of a quite innovative technique based on optic fibers (the reader interested in further details is referred to [42]). In addition, there is also a

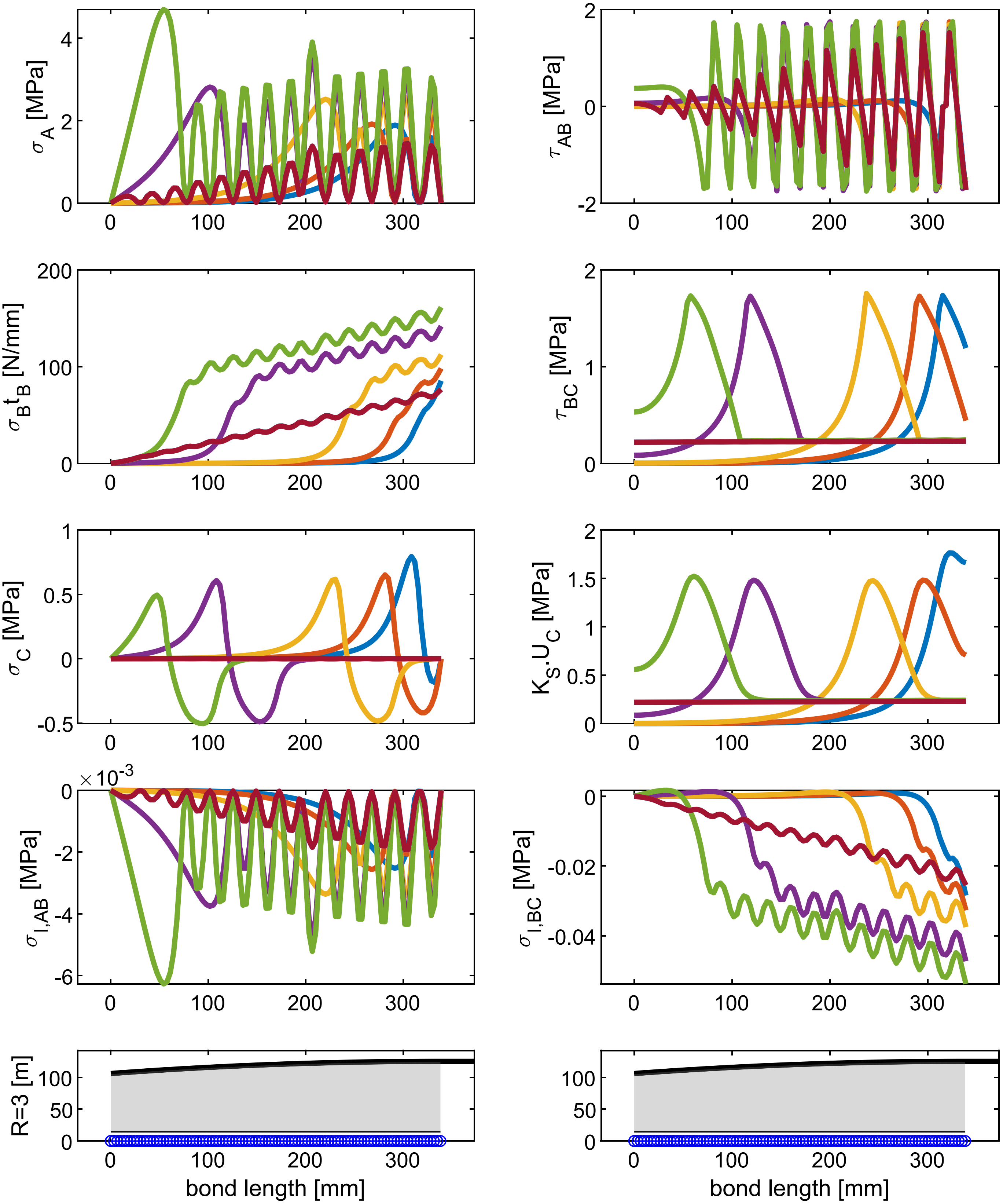

Fig. 13. CBE data. From the top-left in clockwise order. σ_A, τ_{AB}, τ_{BC}, $K_S U_C$, $\sigma_{I,BC}$, $\sigma_{I,AB}$, σ_C, $\sigma_B t_B$ behavior along the bond length (the color of the curves corresponds to the particular instants investigated during the loading process and matches that of the points represented in the previous sub-figure).

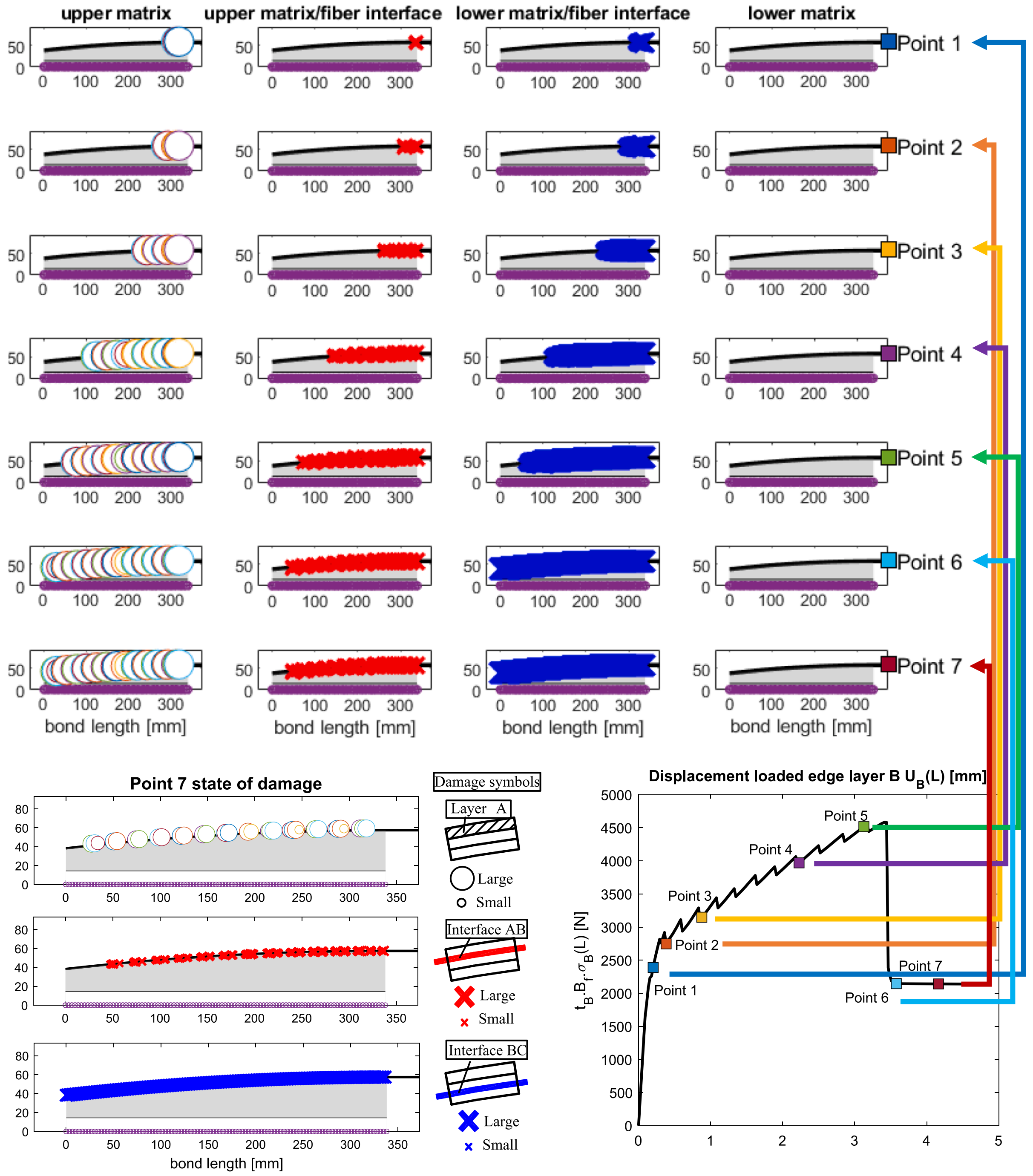

Fig. 14. CBE data. Propagation of damage inside mortar layers and interfaces at the different instants investigated during the loading process. White circles and red/blue crosses represent mortar and interface damage, respectively. Their dimension is proportional to the amount of damage. (For interpretation of the references to color in this figure legend, the reader is referred to the web version of this article.)

wide mechanical characterization of the masonry material constituting the curved pillars, which is not used here because the model does not allow to consider non-linearities in the substrate.

The mechanical and geometrical properties adopted for the different materials characterizing the reinforcement package are summarized in Table 1. In general, they are assumed in strict agreement with those experimentally determined in [43] and those adopted by Grande et al. in [50], who presented a numerical model very similar, but based on a classic Finite Element mono-dimensional discretization. K_s is assumed ten times higher than the value assumed for K_I (the same stiffness is assumed for outer and inner matrix, i.e. $K_I = K_{IAB} = K_{IBC}$), but authors experienced that the elastic deformability of such interface has little influence on the global and local behavior of the numerical model.

Few words should be spent about the out-of-plane width B_F of the reinforcing package, also known as effective width of the reinforcing package. In fact, as already anticipated, in [42] an optic fiber was glued on the central fiber bundle belonging to the same FRCM reinforcing package here considered, but applied on a flat masonry substrate. The aim was to experimentally evaluate the constitutive behavior of the interface between fiber and mortar, but the measure refers exclusively to one fiber bundle. The nominal width is 63 mm, but according to [42] and [43] there are 7 bundles embedded into the mortar layers, each of

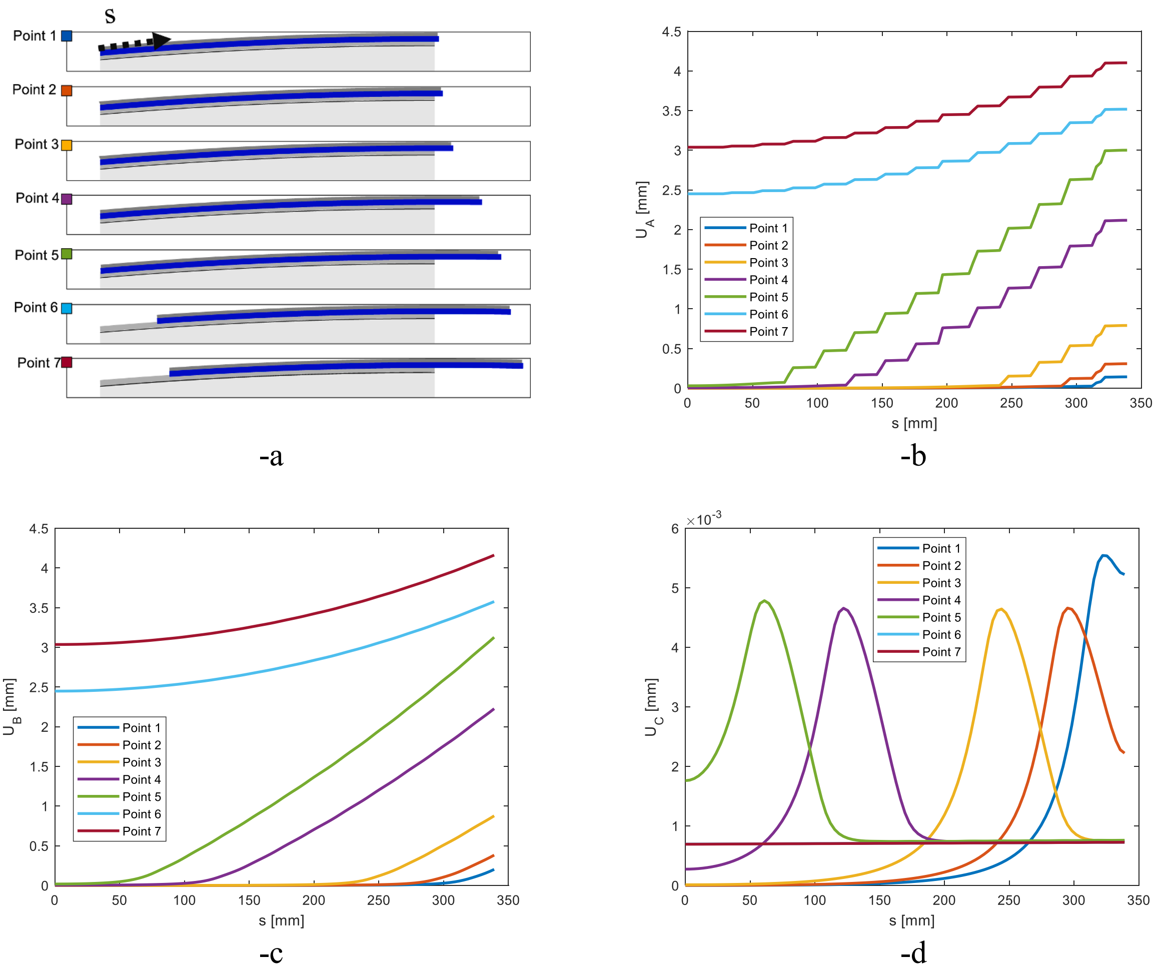

Fig. 15. CBE data. Deformed shapes of the reinforcement package (-a) at 7 values of the displacement $U_B(L)$ applied at the loaded edge. -b: $U_A(s)$ (displacement of the outer matrix layer). -c: $U_B(s)$ (displacement of the fiber). -d: $U_C(s)$ (displacement of the inner matrix layer).

nominal width equal to 4 mm. The effective width B_F (i.e. where tangential stresses are actually exchanged between mortar and fiber) is therefore reasonably equal to 28 mm.

Fig. 5 shows a comparison between experimental data obtained in [42] and the numerical trilinear slip-tangential stress constitutive relation adopted here for the matrix-fiber interfaces to simulate the behavior of the curved specimens. The thick continuous black curve depicted in Fig. 5 corresponds to the numerical data reported in Table 1. As it can be noticed, the agreement between experimental evidence and input parameters of the model for the interfaces AB and BC is quite convincing.

A discretization with $n_e = 200$ subdivisions of the bond length and 100 load steps (under a displacement-based control strategy with applied displacement $U_B(L)$ at the loaded edge of the fiber) is assumed.

The global response of the accounted specimen configurations is depicted in Fig. 6 together with the experimental curves. With reference to Fig. 6, on the horizontal axis the fiber displacement $U_B(L)$ at the loaded edge is represented, whereas on the vertical axis the force applied at the loaded edge $t_B B_F \sigma_B(L)$ is reported. In the same figure, the experimental results are also represented.

As it can be noted, the agreement with experimental data is rather satisfactory. In particular, it is worth noting how, for all the four cases studied, the numerical global curves fall almost everywhere inside the experimental envelope.

The curvature effect on both the ultimate ductility and the peak strength may be easily appreciated, see Fig. 7.

The teeth visible in the pseudo-linear hardening phase after the triggering of the non-linearity at the interfaces (AB & BC) is a consequence of the formation of tensile cracks on the external mortar layer, as it will be discussed in the sequel commenting the global behavior.

The present approach has, in fact, also the advantage of providing a precise local information regarding the propagation of the non-linearity in the different layers. Hereafter, the cases CAE, CBE, CBI and CAI are discussed separately.

- CAE: Extrados reinforcement, high curvature of the substrate

The local behavior is shown in detail in Figs. 8-11. In particular, Fig. 8 depicts the trend of the kinematic variables (displacements U_A, U_B, U_C of A-C layers and jumps of displacements at the fiber-mortar interfaces , $U_B - U_C$ and $U_B - U_A$) along the bond length, at 7 different meaningful steps of the loading process. The global curves, represented by the force $t_B B_f \sigma_B(L)$ applied at the loaded edge versus the displacements $U_B(L)$, $U_B(0)$ of layer B at the loaded and free edge respectively, are plotted in the bigger sub-figure. The previously mentioned steps are identified with squares filled with different colors. The curves depicted in each sub figure and representing the kinematic variables are plotted with the same colors used to identify the 7 steps and therefore match those of the squares represented in the top-left sub-figure of Fig. 8. In other words, each curve is represented with a different color. It depicts the local behavior (a displacement in this case) along the bond length at a certain instant identified by the label Point 1-Point 7, and represented in the global curve by a square filled with the same color. Different

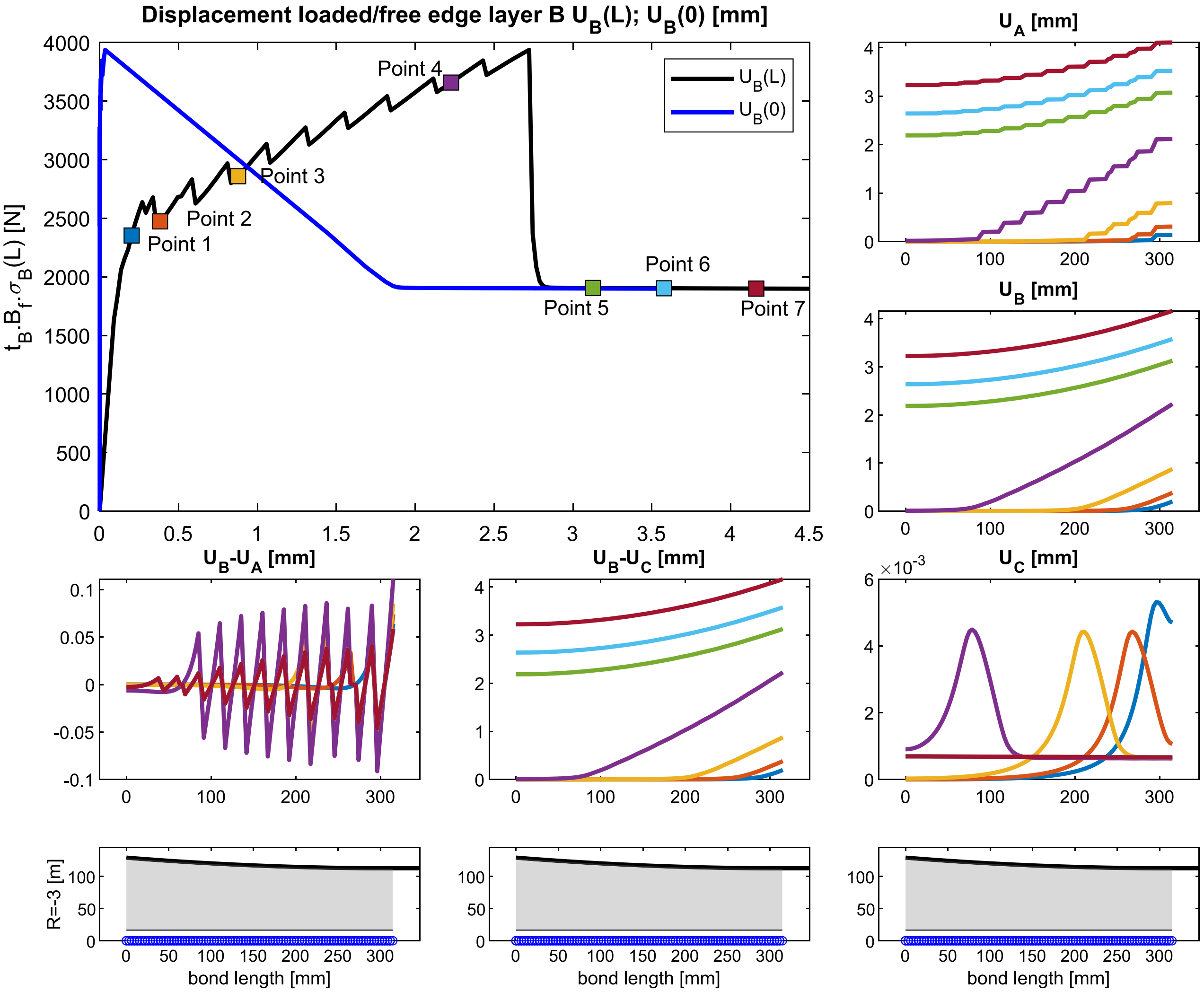

Fig. 16. CBI data. From the top-left in clockwise order. Force $t_B B_f \sigma_B(L)$ - displacement $U_B(L)$, $U_B(0)$ curves; U_A, U_B, U_C, $U_B - U_C$, $U_B - U_A$ behavior along the bond length (the color of the curves corresponds to the particular instants investigated during the loading process and matches that of the points represented in the top-left sub-figure).

colors are used to facilitate the reading of the results obtained. Fig. 9 follows the same rationale of Fig. 8, but it depicts the static variables, namely (in clockwise order starting from the top-left sub-figure) σ_A, τ_{AB}, τ_{BC}, $K_S U_C$, $\sigma_{I,BC}$, $\sigma_{I,AB}$, σ_C, $\sigma_B t_B$.

Fig. 10 represents at the same steps, the propagation of damage inside mortar layers and at interfaces between mortar and fiber. White circles and red/blue crosses represent the mortar and interface damage, respectively. Red color is used for the upper interface, whereas blue color for the lower one. The dimension of the symbols is directly proportional to the amount of damage, so bigger circles and crosses mean higher damage. As can be noted from the zoomed detail of the last instant investigated (Point 7, when the reinforcement is fully debonded), the external mortar layer cracks in several points, localizing the damage. The outer interface, because directly connected to the cracked layer, enters in the inelastic phase, but only within two contiguous cracks of the outer mortar, so with a value of damage relatively small. On the contrary, the inner mortar/matrix interface, which is free to damage because of the state of compression of the inner mortar, delaminates more and moves rapidly the debonded front from the loaded edge to the free one. Fig. 11 depicts the (suitably amplified) deformed shapes of the different layers. Quantitative plots of the displacements occurring in Layers A, B,C at different instants are also reported. It is interesting to notice that the distribution of the displacements on Layer A is characterized by a stepped shape. Each pseudo-horizontal plateau corresponds to a crack. Layer B displacements are quite close to Layer A ones, but more regular, because of the elastic assumption made for Layer B. Layer C displacements are much smaller than those observed in Layer A and B. Such behavior of the model also suggests that to lump the nonlinearity exclusively at the interface between Layers B and C (as proposed for instance in [19]) is certainly a simplification, but still grounded on a reasonable physical interpretation of the debonding phenomenon.

Especially Fig. 10 and Fig. 11 are quite self-explaining about the debonding triggered, which occurs initially for the inelastic slippage of the fiber net with respect to both upper and lower mortar layers, near the loaded edge. Both interfaces move the damage front towards the free edge and contemporarily the upper mortar layer starts to spread diffused cracks from the right to the left. Full debonding occurs with the lower mortar layer intact, with both interfaces considerably damaged and with the upper mortar layer entirely cracked in tension.

Fig. 9 is particularly interesting, especially as far as the distributions of $\sigma_{I,AB}$ and $\sigma_{I,BC}$ are concerned. $\sigma_{I,BC}$ attains in the inelastic phase (from Point 3 to Point 7, all located in the pseudo-linear post elastic branch of the global curve) compression values of about −0.1 MPa, starting from the loaded edge and progressively moving the front from the right to the left. On the contrary, the normal stress $\sigma_{I,AB}$ at the external interface,

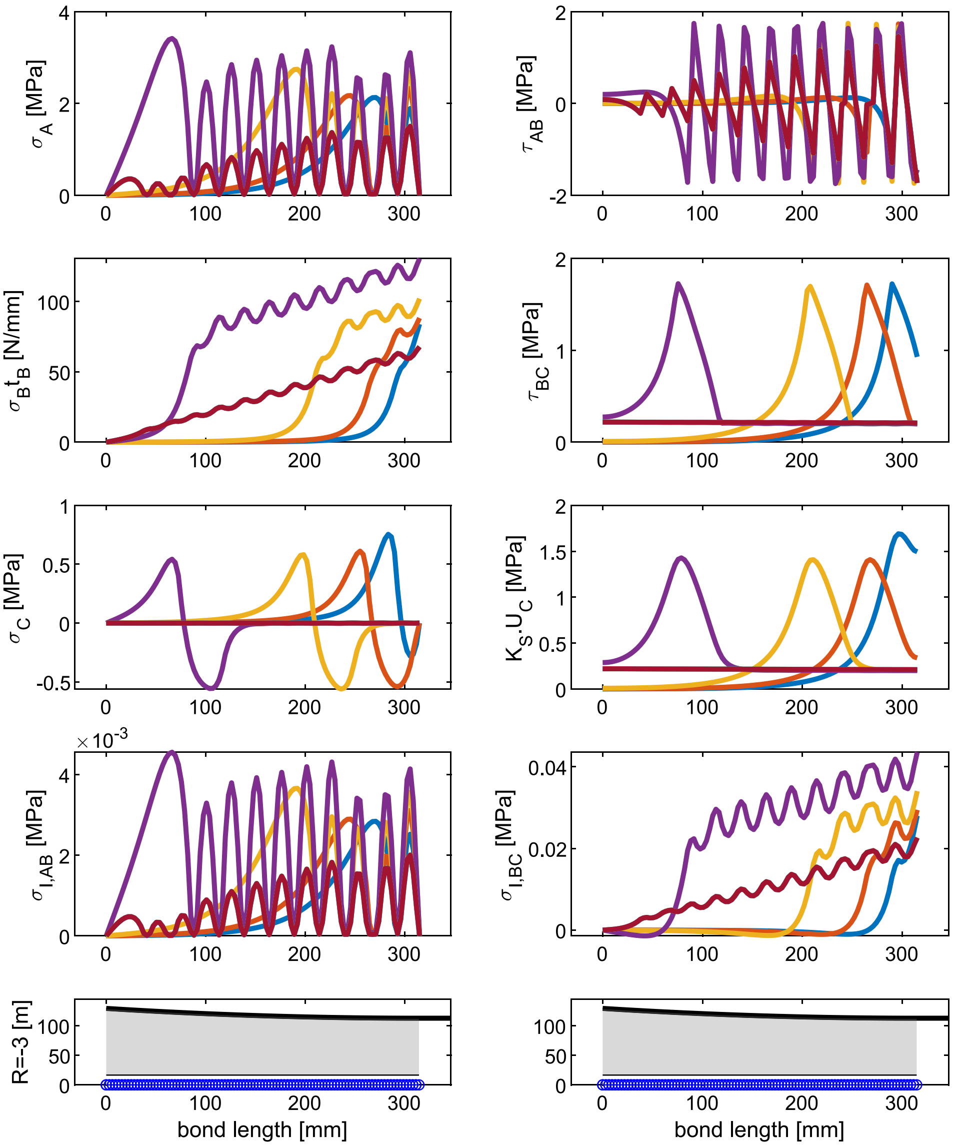

Fig. 17. CBI data. From the top-left in clockwise order. σ_A, τ_{AB}, τ_{BC}, $K_S U_C$, $\sigma_{I,BC}$, $\sigma_{I,AB}$, σ_C, $\sigma_B t_B$ behavior along the bond length (the color of the curves corresponds to the particular instants investigated during the loading process and matches that of the points represented in the previous sub-figure).

remains in practice negligible. The internal interface becomes therefore more ductile and more resistant, and it can be concluded that its role on the global behavior observed is crucial. The extra resistance and extra ductility observed experimentally for an extrados reinforcement at high curvature of the substrate is mainly a consequence of the improved mechanical properties of the internal (BC) interface, induced by the presence of compression stresses. Such conclusion is confirmed by the propagation of damage inside the interfaces during the loading process (see Fig. 10). Both interfaces, indeed, are subjected by an inelastic slippage, but the damage is higher for the external interfaces, a feature confirmed by the bigger dimension of the red crosses when compared with that of the blue ones.

- CBE: Extrados reinforcement, low curvature of the substrate

The same rationale used for CAE to represent the local behavior is adopted to discuss the results obtained for CBE, which are shown from Figs. 12-15.

In particular, Fig. 12 depicts the global behavior, identifying again 7 meaningful steps during the whole loading process (the same colors used for CBE are adopted), along with the distribution of the kinematic variables throughout the bond length. Fig. 13 shows the static variables, Fig. 14 depicts the damage propagation and Fig. 15 represents the magnified deformed shape.

The process of debonding is identical to that observed for CAE. The zigzagging shape of $U_B - U_A$ (Fig. 13) helps in identifying the position of the cracks forming in the external mortar layer, a feature confirmed by the shape of the normal stresses in layer A (Fig. 13). The smooth shape of τ_{BC} in the same figure indirectly suggests that the internal mortar layer C remains in the elastic phase. It is interesting also to point out that the layer C is in some regions of the bonded length in compression and in others in tension, but the peak positive values of the normal stress remain far under the ultimate strength in tension. The failure mechanism forming, understandable by the damage propagation (Fig. 14) and the deformed shape (Fig. 15) is essentially identical to that observed for CAE. It is in fact characterized by the inelastic slippage of the internal fiber net with respect to both the external and internal matrix layers. Layer A progressively cracks from the loaded edge towards the free one, but with a crack width smaller than that observed for CAE, as confirmed by the smaller size of the circles representing the cracks (Fig. 14).

Analogously to Fig. 9, it is particularly interesting to comment the distributions of interface normal stresses $\sigma_{I,AB}$ and $\sigma_{I,BC}$ shown in Fig. 14.

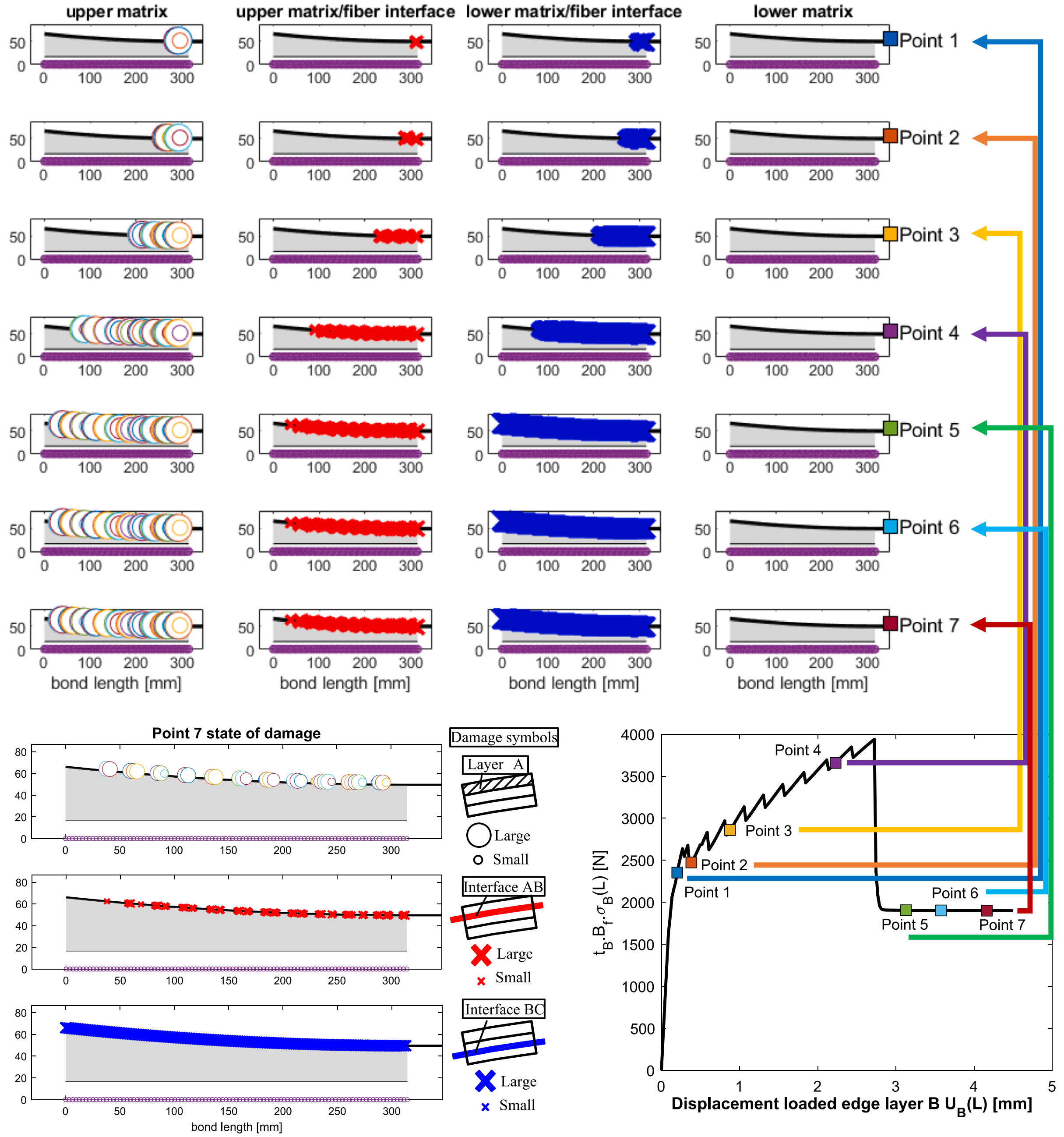

Fig. 18. CBI data. Propagation of damage inside mortar layers and interfaces at the different instants investigated during the loading process. White circles and red/blue crosses represent mortar and interface damage, respectively. Their dimension is proportional to the amount of damage. (For interpretation of the references to color in this figure legend, the reader is referred to the web version of this article.)

Indeed, $\sigma_{I,BC}$ attains compression values of about −0.4, −0.5 MPa near the loaded edge. Such compression state is lower than that observed for CAE and attained later (Points 4 & 5). The length of the interval where such values are observed is more limited and localized near the loaded edge. Consequently, the internal interface is sensibly less resistant and less ductile, a feature which justifies the more performant global behavior of a reinforcement applied at the extrados of a pillar with higher curvature. On the contrary, the normal stress $\sigma_{I,AB}$ at the external interface remains again negligible.

- CBI: Intrados reinforcement, low curvature of the substrate

Local results (intending with this term the trend of the internal variables throughout the bonded length and the evolution of damage) for the intrados reinforcement on pillars at low curvature of the substrate are summarized from Figs. 16-19.

From an overall analysis of the results, cracks appear progressively on the extrados matrix layer (see the slip trend $U_B - U_A$ in Fig. 16, the tangential stress at the interface τ_{AB} in Fig. 17 or the damage evolution of the upper layer A depicted in Fig. 18, left column). Contemporarily, the internal fiber layer B slips inelastically with respect to both internal and external matrix layers, see Fig. 18 central columns. Looking at the deformed shapes of Fig. 19, the fiber (layer B) and the cracked matrix layer A slip together over the internal matrix (layer C), which remains elastic and almost rigidly connected to the substrate (thanks to the relatively high value of stiffness assigned to K_S). The trend of the displacement U_A along the bonded length (Fig. 16) is characterized by several steps, corresponding to the formation of the concentrated cracks

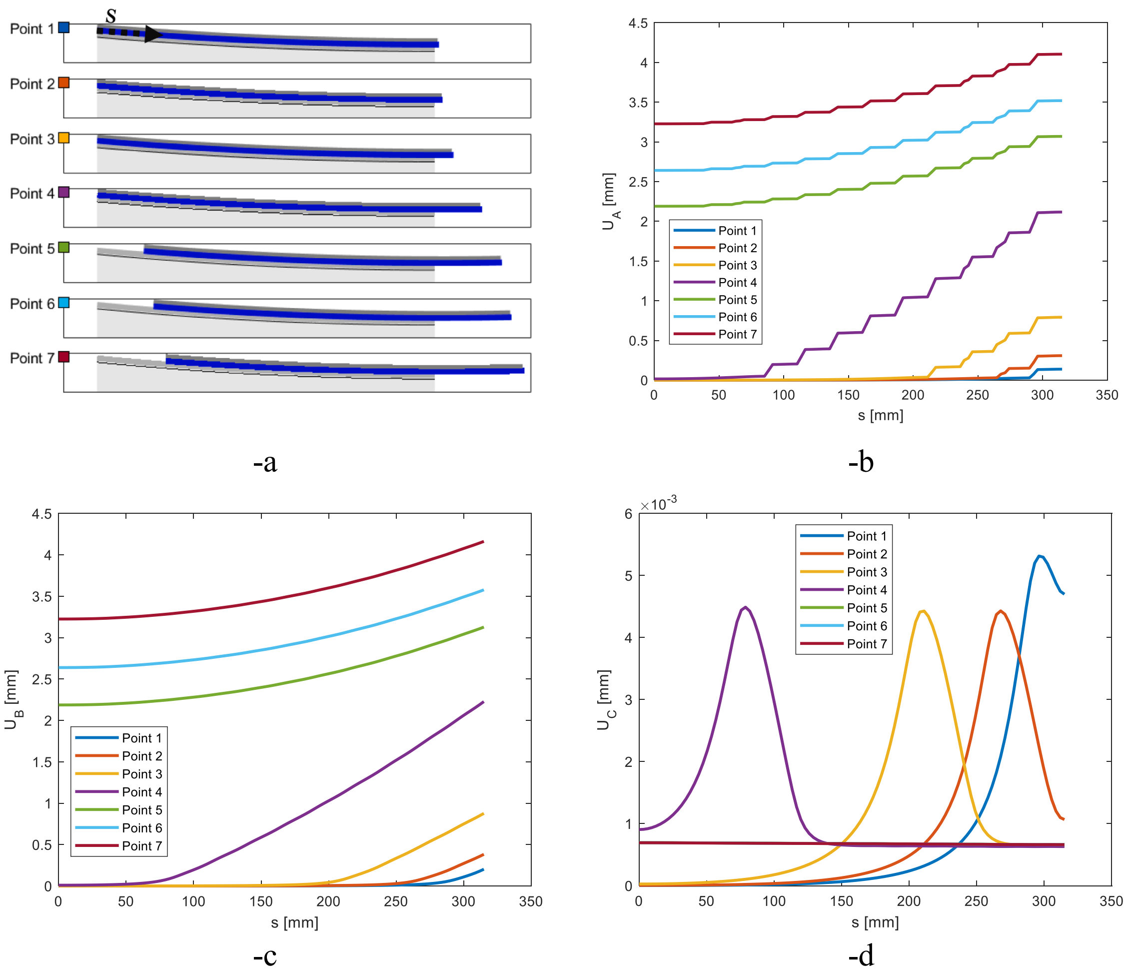

-a -b

-c -d

Fig. 19. CBI data. Deformed shapes of the reinforcement package (-a) at 7 values of the displacement $U_B(L)$ applied at the loaded edge. -b: $U_A(s)$ (displacement of the outer matrix layer). -c: $U_B(s)$ (displacement of the fiber). -d: $U_C(s)$ (displacement of the inner matrix layer).

on the layer A.

Regarding the internal interface BC, normal stress reaches in the inelastic pseudo-linear branch values of about 0.05 MPa (see Fig. 17), a feature which reduces both the global ductility and the peak strength of the reinforced system.

- CAI: Intrados reinforcement, high curvature of the substrate

The trend of the internal variables, kinematic and static, at 7 different steps of the loading process are depicted for CAI specimens (reinforcement at the intrados with high curvature of the substrate) respectively in Fig. 20 and Fig. 21.

Analogously to the previous three cases, the damage evolution on matrix layers A & C of the reinforcing pack and at the interfaces AB and BC between matrix and fiber are reported in Fig. 22. Finally, Fig. 23 shows the deformed shapes obtained numerically, suitably amplified to have a more precise insight into the failure mechanism triggered.

No particular differences with respect to the previous cases can be appreciated. There is an inelastic slippage of the internal layer B with respect to matrix layers A & C, propagating from the loaded edge and progressively moving the inelastic front from the right to the left. Contemporarily, the external matrix layer A starts to crack. In correspondence of the full debonding, the external matrix appears fully cracked and slides inelastically together with layer B with respect to the undamaged internal matrix layer.

Regarding the internal interface BC, normal stresses reach, in the inelastic pseudo-linear branch, values of around 0.1 MPa (see Fig. 17). Therefore, both the strength and the ductility of the internal interface drop down (also with respect to the CBI case), resulting in a quite visible reduction of the load carrying capacity and the global ductility, see Fig. 6 and Fig. 7.

4. Synoptical physical Considerations: Comparison with experimental evidence

Globally, it has been shown that the experimental load–displacement outcome can be predicted in a satisfactory way with the model proposed. Such feature is crucial, considering also the main aim of the approach proposed, i.e. the utilization at structural level of 1D truss finite elements perfectly bonded to the substrate and obeying a fictitious constitutive behavior reflecting the debonding in laboratory samples. It is however also interesting to investigate further how the model can reproduce the actual local behavior. This is not an easy task, because the presence of the outer mortar layer does not allow to use consolidated experimental approaches able to give information on the local state of stress inside the different layers. FRCM is in fact more complex than FRP, and sophisticated experimental measures, for instance based on optic-fibers [42], should be adopted. In any case, from a simple observation of the propagation of cracks before and near failure, some interesting information can be gathered in any case. The experimental failure modes for all the configurations inspected are characterized by a visible slippage of the internal and external mortar/fiber interfaces, see Fig. 24

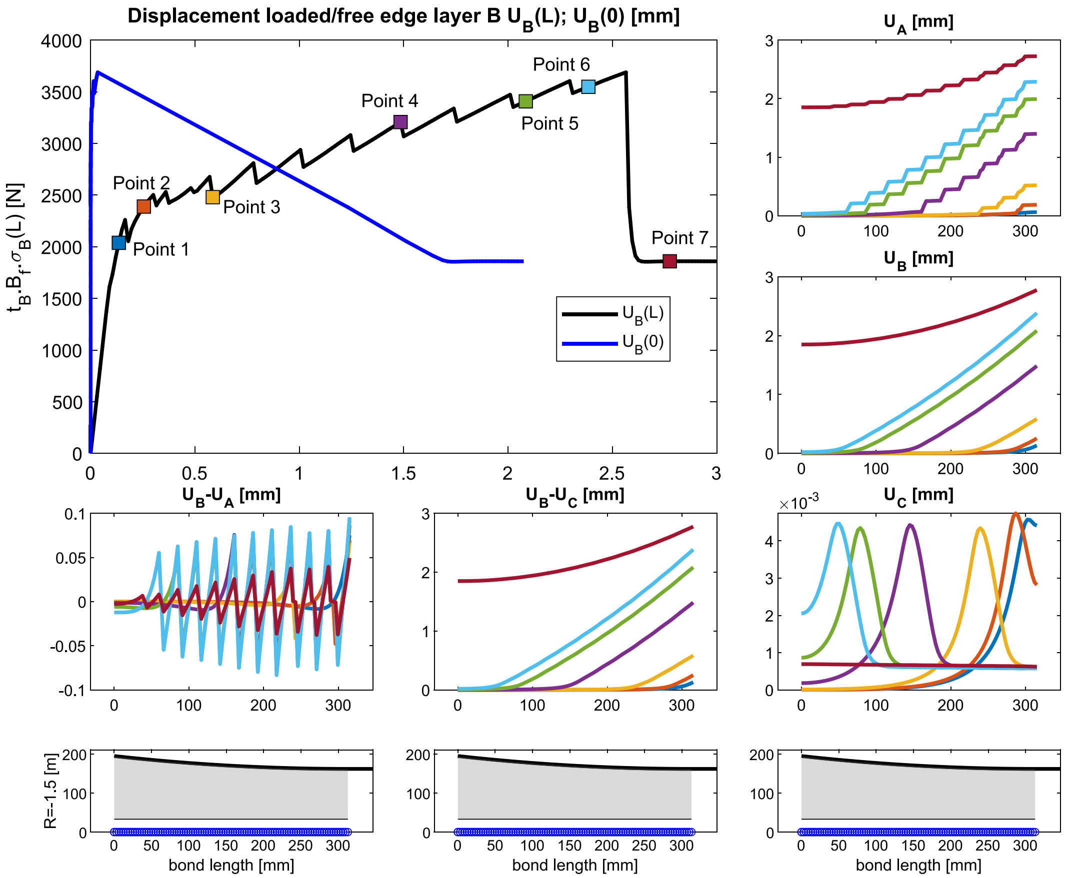

Fig. 20. CAI data. From the top-left in clockwise order. Force $t_B B_f \sigma_B(L)$ - displacement $U_B(L)$, $U_B(0)$ curves; U_A, U_B, U_C, $U_B - U_C$, $U_B - U_A$ behavior along the bond length (the color of the curves corresponds to the particular instants investigated during the loading process and matches that of the points represented in the top-left sub-figure).

(extrados reinforcement CAE and CBE) and Fig. 25 (intrados reinforcement, CAI and CBI). The external mortar layer cracks in any case. Both phenomena are correctly reproduced by the model proposed. In fact, in Figs. 24 and 25, also the profiles numerically obtained of the internal interface (BC) and the axial fiber stress multiplied by layer B thickness (in other words the fiber layer force divided by its width) are represented at increasing values of displacement applied at the loaded edge. It is quite evident the progressive advancement of the delamination front, from the loaded edge to the free one. In fact, the peak tangential stress of the BC interface observed in the numerical model progressively moves from the loaded edge to the free one. Accordingly, the tensile stress in the fiber layer in the de-bonded part grows globally in a linear way, with some sinusoidal oscillations consequence of the cracks forming in the external layer. The global linear increase of the fiber stress in the de-bonded region is a consequence of the residual strength of the mortar/fiber interface. There are some differences passing from the extrados to the intrados reinforcement. The most evident is that debonding occurs more rapidly for the intrados reinforcement, with an obvious reduction of load carrying capacity and ductility. This notwithstanding, the failure mechanism observed is always the same, i.e. delamination of the mortar-fiber interfaces and formation of cracks in the outer mortar layer. The experimental results are quite clear in this regard, and the numerical model -albeit its intrinsic simplifications- can correctly reproduce the experimental outcome.

5. Conclusions

The recent scientific literature reports some contributions concerning the numerical study of the bond behavior of FRCM strengthening systems externally applied to curved masonry structures. In this context, the present paper proposed an innovative semi-analytical model able to simulate the bond behavior of FRCM systems applied at the extrados or intrados of curved masonry elements. The model consisted of assuming the strengthening system composed of three separate and superimposed layers, namely the fiber grid (i.e. the reinforcement) embedded into an upper and lower matrix. The reinforcement was assumed elastic, whereas the lower and upper matrix layers were modeled by considering a linear-elastic relationship followed by a softening phase. The three components of the strengthening system were assumed in a monoaxial state of stress, interacting mutually by means of interfaces subjected to both shear and normal stresses. The tangential stress-slip relationship of the interfaces was assumed characterized by a non-linear law with softening. The peak tangential strength and the ductility were also assumed dependent on the actual normal stress acting at the interface, via a classic Mohr-Coulomb criterion. The kinematic and static internal variables were the axial displacements and the normal stresses of the layers, respectively. The lower matrix was connected to the substrate by a further interface characterized by a linear-elastic behavior. Under such assumptions, a system of first order nonlinear differential equations was derived and subsequently solved in closed form.

An experimental dataset obtained by the Authors for small masonry pillars reinforced with FRCM and characterized by 4 different curvatures was selected to estimate the accuracy of the proposed model, which showed an excellent reliability in reproducing both the global and local behavior.

Future developments of the model here proposed should move towards the introduction of possible states of pre or post-damage involving the masonry support. This will be particularly useful in case of damaged structures or in case of weak materials composing the masonry substrate. Furthermore, the role played by mortar joints, which typically

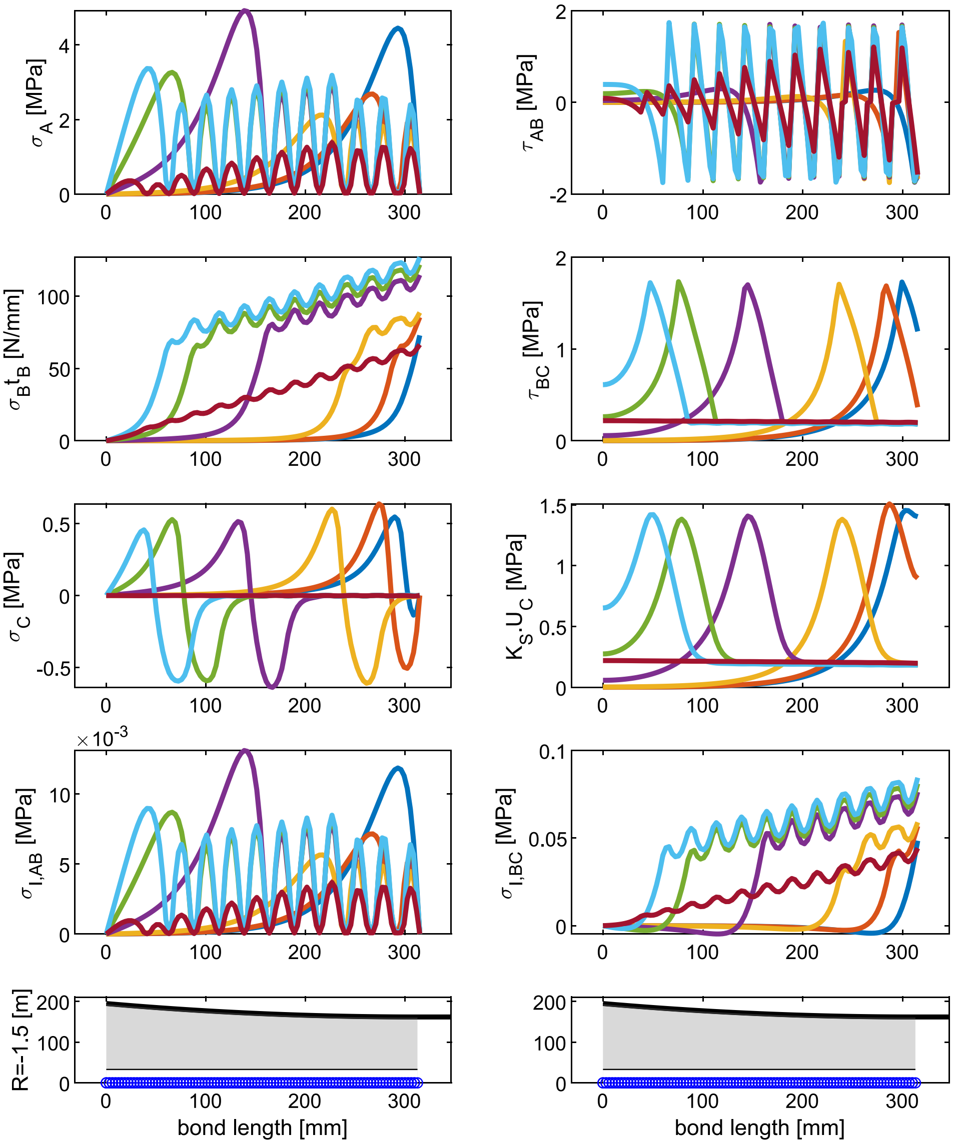

Fig. 21. CAI data. From the top-left in clockwise order. σ_A, τ_{AB}, τ_{BC}, $K_S U_C$, $\sigma_{I,BC}$, $\sigma_{I,AB}$, σ_C, $\sigma_B t_B$ behavior along the bond length (the color of the curves corresponds to the particular instants investigated during the loading process and matches that of the points represented in the previous sub-figure).

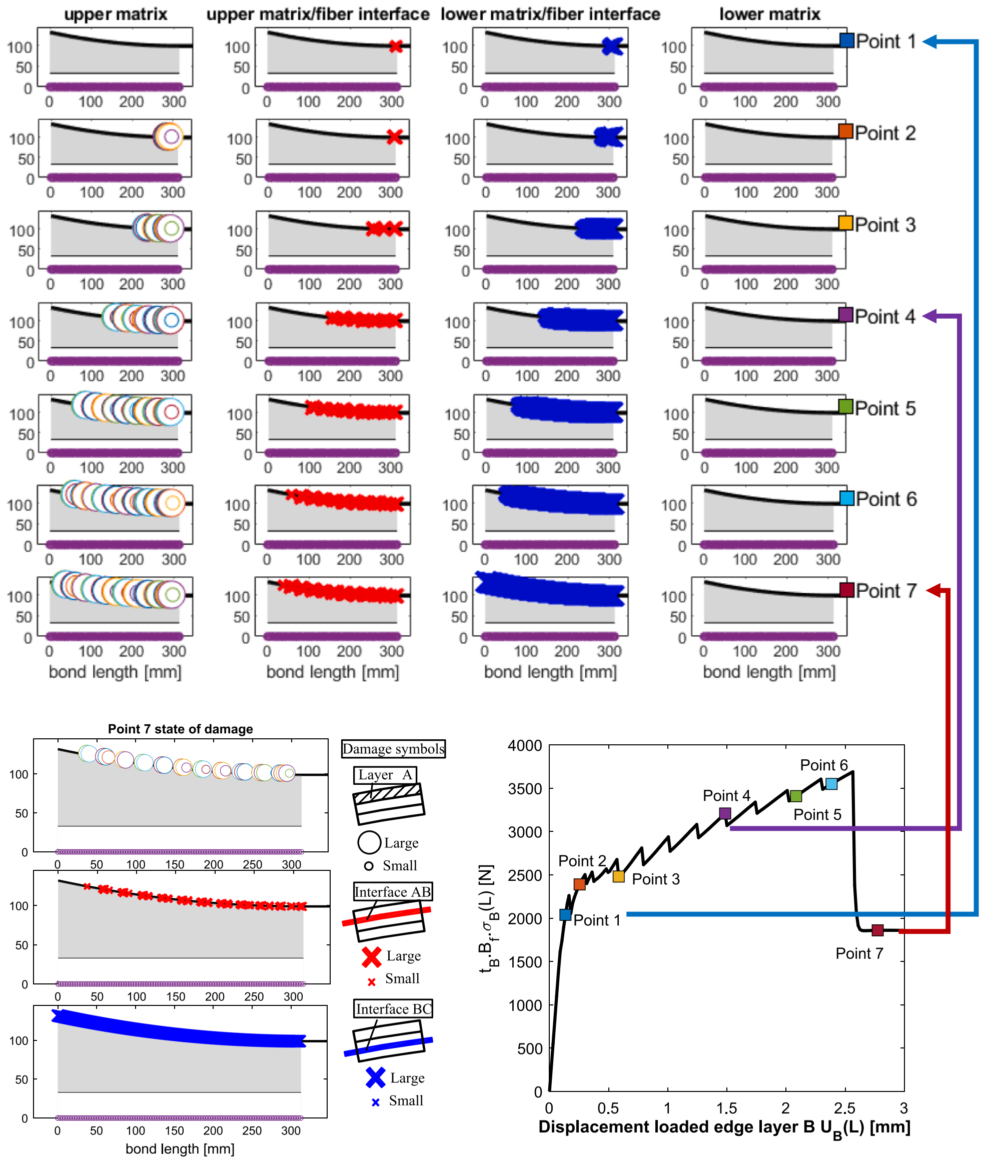

Fig. 22. CAI data. Propagation of damage inside mortar layers and interfaces at the different instants investigated during the loading process. White circles and red/blue crosses represent mortar and interface damage, respectively. Their dimension is proportional to the amount of damage. (For interpretation of the references to color in this figure legend, the reader is referred to the web version of this article.)

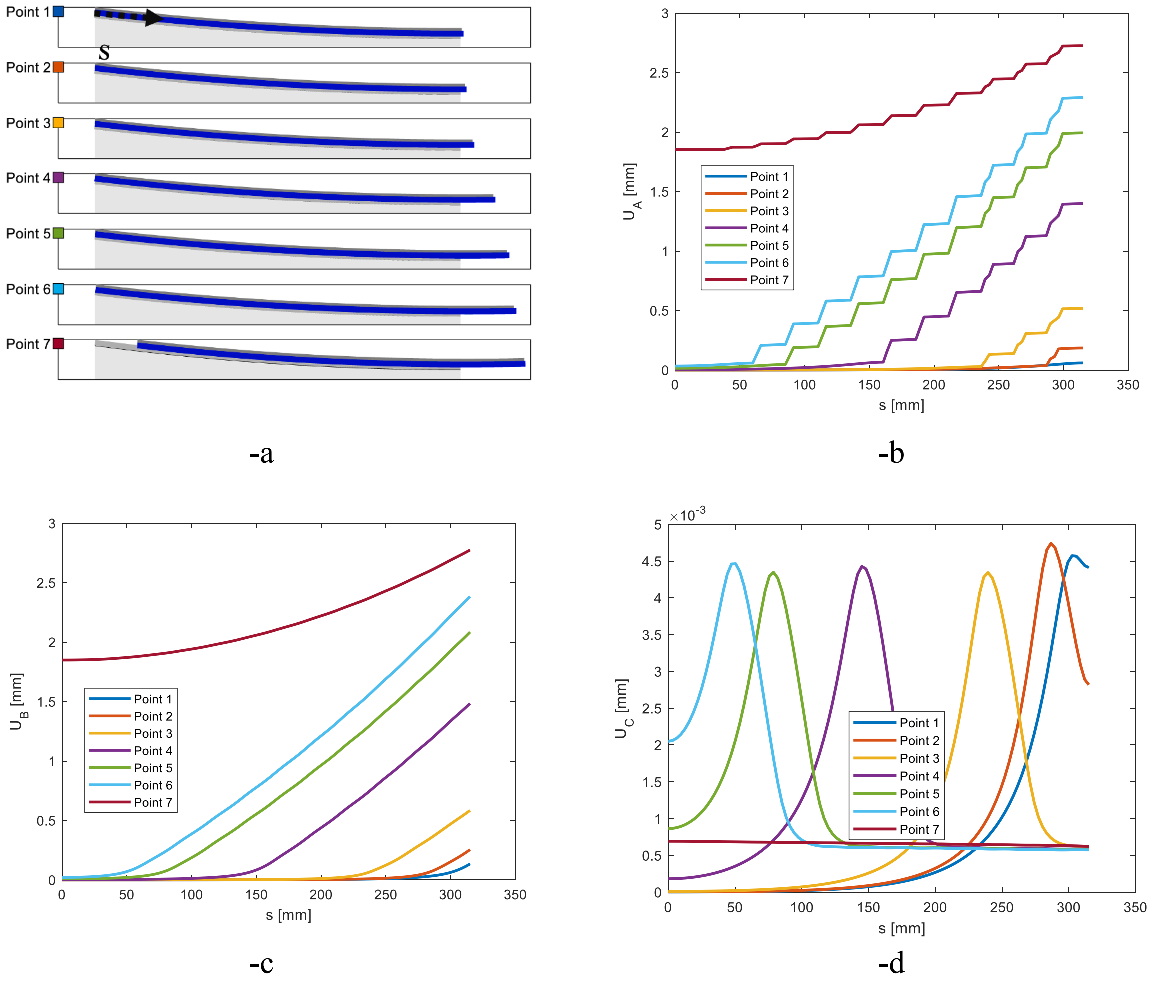

-a

-b

-c

-d

Fig. 23. CAI data. Deformed shapes of the reinforcement package (-a) at 7 values of the displacement $U_B(L)$ applied at the loaded edge. -b: $U_A(s)$ (displacement of the outer matrix layer). -c: $U_B(s)$ (displacement of the fiber). -d: $U_C(s)$ (displacement of the inner matrix layer).

exhibit very poor mechanical properties in historical masonry, deserves future dedicated investigation.

The major advantage of the approach proposed is its immediate implementation as a pre-processing kernel, useful to tune fictitious mechanical properties of perfectly bonded non-linear truss elements to apply in standard FE codes for the simulation of an FRCM reinforcement. In principle, this would allow to numerically analyze real scale structures, where the utilization of analytical approaches is not possible, in a more effective way. Indeed, fast sensitivity analyses can be carried out, thus avoiding all those issues (e.g. premature halting, lack of convergence, too many parameters to choose, long processing times, etc.) that a common user is frequently asked to face with in standard FE computations. The major limitation stands in the native mono-axial nature of the model (for instance, spalling is not reproducible), the assumption of an elastic behavior for the FRCM/substrate interface and the infinite resistance of the substrate. The first limitation is intrinsic and cannot be eliminated. For the second issue, an experimental work aimed at identifying the non-linear properties of the FRCM-substrate interface would be necessary, but the research is at present in its embryonic stage. On the contrary, for the third matter, it is always possible at a structural level to model the substrate as elasto-damaging, still applying on the surface trusses perfectly bonded with a conventional non-linear behavior, deduced from the results obtained by means of the present approach applied on small specimens.

CRediT authorship contribution statement

Gabriele Milani: Conceptualization, Data curation, Formal analysis, Investigation, Methodology, Software, Validation, Visualization, Writing – original draft, Writing – review & editing. **Ernesto Grande:** Conceptualization, Data curation, Formal analysis, Investigation, Methodology, Validation, Visualization, Writing – original draft, Writing – review & editing. **Tommaso Rotunno:** Conceptualization, Data curation, Formal analysis, Investigation, Methodology, Validation, Visualization, Writing – original draft, Writing – review & editing. **Mario Fagone:** Conceptualization, Data curation, Formal analysis, Investigation, Methodology, Validation, Visualization, Writing – original draft, Writing – review & editing.

Declaration of competing interest

The authors declare that they have no known competing financial interests or personal relationships that could have appeared to influence the work reported in this paper.

Data availability

Data will be made available on request.

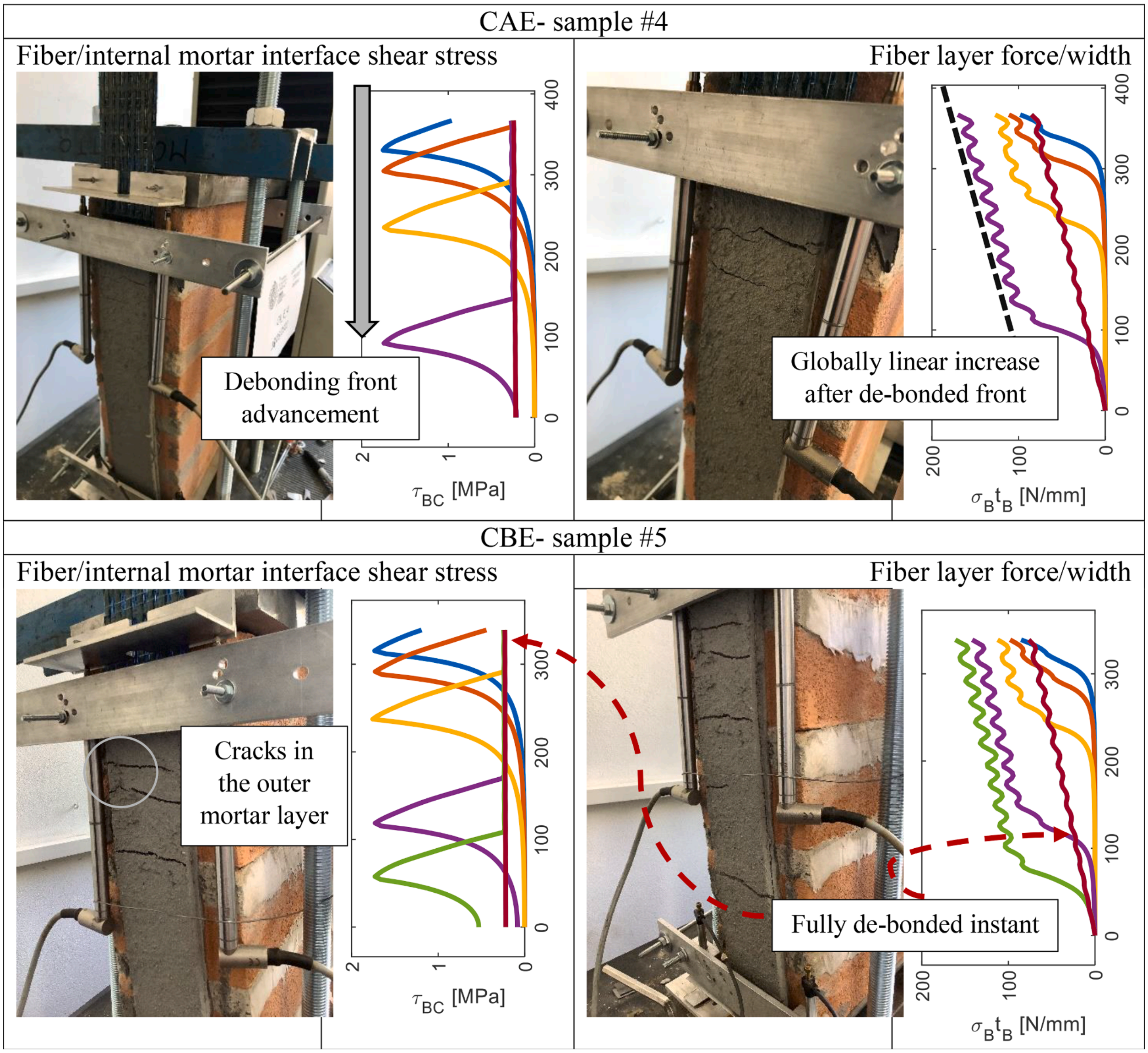

Fig. 24. CAE and CBE samples. Comparison between numerical prediction and experimental damage propagation.

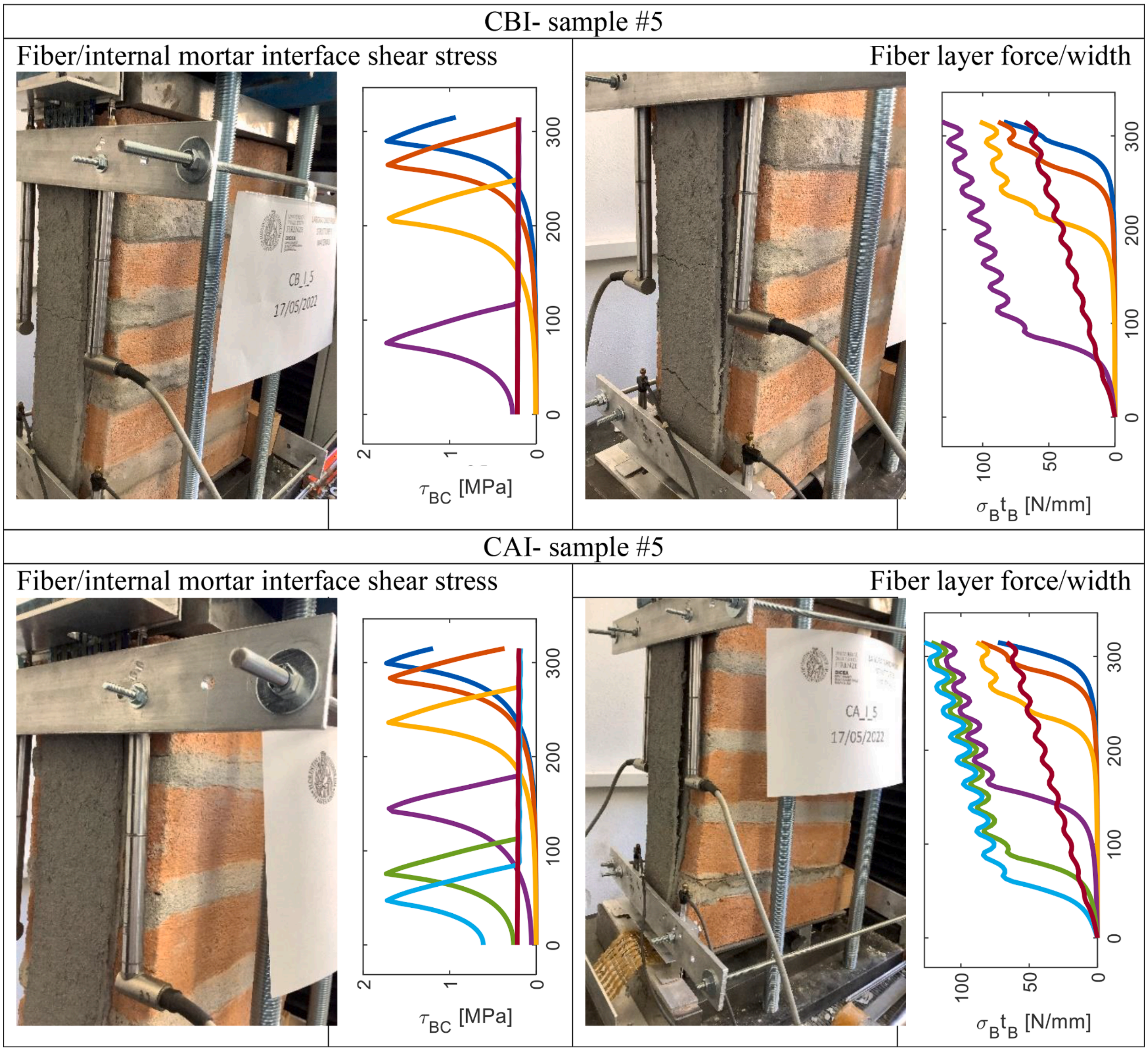

Fig. 25. CAE and CBE samples. Comparison between numerical prediction and experimental damage propagation.

References

[1] Papanicolaou CG, Triantafillou TC, Karlos K, Papathanasiou M. Textile-reinforced mortar (TRM) versus FRP as strengthening material of URM walls: in-plane cyclic loading. Mater Struct 2007;40:1081–97. https://doi.org/10.1617/s11527-006-9207-8.

[2] Toutanji H, Deng Y. Comparison between organic and inorganic matrices for RC beams strengthened with carbon fiber sheets. J Compos Constr 2007;11(5):507–13.

[3] Nanni A. A new tool for concrete and masonry repair – strengthening with fiber-reinforced cementitious matrix composites. Concr Inter 2012;34:43–9.

[4] de Felice G, De Santis S, Garmendia L, Ghiassi B, Larrinaga P, Lourenço PB, et al. Mortar-based systems for externally bonded strengthening of masonry. Mater Struct 2014;47(12):2021–37.

[5] Ghiassi B. Mechanics and durability of lime-based textile reinforced mortars. RILEM Technical Letters 2019;4:130–7. https://doi.org/10.21809/rilemtechlett.2019.99.

[6] Ascione L, de Felice G, De Santis S. A qualification method for externally bonded fibre reinforced cementitious matrix (FRCM) strengthening systems. Compos B 2015;78:497–506.

[7] De Santis S, Hadad HA, De Caso y Basalo F, de Felice G, Nanni A. Acceptance criteria for tensile characterization of fabric-reinforced cementitious matrix systems for concrete and masonry repair. J. Compos. Constr. 2018;22(6): 04018048. https://doi.org/10.1061/(ASCE)CC.1943-5614.0000886.

[8] D'Ambrisi A, Feo L, Focacci F. Experimental analysis on bond between PBO FRCM strengthening materials and concrete. Compos Part B-Eng 2013;44(1):524–32.

[9] Carloni C, D'Antino T, Sneed LH, Pellegrino C. Role of the matrix layers in the stress-transfer mechanism of FRCM composites bonded to a concrete substrate. J Eng Mech 2014;141(6):#04014165.

[10] D'Antino T, Sneed LH, Carloni C, Pellegrino C. Influence of the substrate characteristics on the bond behavior of PBO FRCM-concrete joints. Constr Build Mater 2015;101:838–50.

[11] De Santis S, Ceroni F, de Felice G, Fagone M, Ghiassi B, Kwiecień A, et al. Round Robin test on tensile and bond behaviour of steel reinforced grout systems. Compos B Eng 2017;127:100–20. https://doi.org/10.1016/j.compositesb.2017.03.052.

[12] Ombres L, Mancuso N, Mazzuca S, Verre S. Bond between Carbon fabric-reinforced cementitious matrix and masonry substrate. J Mater Civ Eng 2019;31:04018356. https://doi.org/10.1061/(ASCE)MT.1943-5533.0002561.

[13] Bertolesi E, Fagone M, Rotunno T, Grande E, Milani G. Experimental characterization of the textile-to-mortar bond through distributed optical sensors. Constr Build Mater 2022;326:126640. https://doi.org/10.1016/j.conbuildmat.2022.126640.

[14] D'Ambrisi A, Feo L, Focacci F. Experimental and analytical investigation on bond between Carbon-FRCM materials and masonry. Compos Part B-Eng 2013;46: 15–20.

[15] Grande E, Imbimbo M, Sacco E. Investigation on the bond behavior of clay bricks reinforced with SRP and SRG strengthening systems. Mater Struct 2015;48(11): 3755–70.

[16] Carozzi FG, Colombi P, Fava G, Poggi C. A cohesive interface crack model for the matrix-textile debonding in FRCM composites. Compos Struct 2016;143:230–41.

[17] D'Antino T, Colombi P, Carloni C, Sneed LH. Estimation of a matrix-fiber interface cohesive material law in FRCM-concrete joints. Compos Struct 2018;193:103–12. https://doi.org/10.1016/j.compstruct.2018.03.005.

[18] Calabrese AS, Colombi P, D'Antino T. Analytical solution of the bond behavior of FRCM composites using a rigid-softening cohesive material law. Compos B Eng 2019;174:1–10. https://doi.org/10.1016/j.compositesb.2019.107051.

[19] Zou X, Sneed LH, D'Antino T. Full range behavior of fiber reinforced cementitious matrix (FRCM)-concrete joints using a trilinear bond-slip relationship. Compos Struct 2020;239:#112024.

[20] Calabrese AS, D'Antino T, Colombi P. Experimental and analytical investigation of PBO FRCM-concrete bond behavior using direct and indirect shear test set-ups. Compos Struct 2021;267.. https://doi.org/10.1016/j.compstruct.2021.113672.

[21] Bertolli V, D'Antino T. Modeling the behavior of externally bonded reinforcement using a rigid-trilinear cohesive material law. Int J Solids Struct 2022;248:111641. https://doi.org/10.1016/j.ijsolstr.2022.111641.

[22] Grande E, Imbimbo M, Sacco E. Numerical investigation on the bond behavior of FRCM strengthening systems. Compos B Eng 2018;145:240–51. https://doi.org/10.1016/j.compositesb.2018.03.010.

[23] Grande E, Milani G. Interface modeling approach for the study of the bond behavior of FRCM strengthening systems. Compos B Eng 2018;141:221–33. https://doi.org/10.1016/j.compositesb.2017.12.052.

[24] Milani G, Grande E. Simple bisection procedure in quickly convergent explicit ODE solver to numerically analyze FRCM strengthening systems. Compos B Eng 2020;199:108322. https://doi.org/10.1016/j.compositesb.2020.108322.

[25] Grande E, Milani G. Procedure for the numerical characterization of the local bond behavior of FRCM. Compos Struct 2021;258:113404. https://doi.org/10.1016/j.compstruct.2020.113404.

[26] Grande E, Milani G, Imbimbo M. Theoretical model for the study of the tensile behavior of FRCM reinforcements. Constr Build Mater 2020;236:#117617.

[27] Grande E, Imbimbo M, Sacco E. Bond behaviour of CFRP laminates glued on clay bricks: Experimental and numerical study. Compos B Eng 2011;42(2):330–40.

[28] Carozzi FG, Milani G, Poggi C. Mechanical properties and numerical modeling of fabric reinforced cementitious matrix (FRCM) systems for strengthening of masonry structures. Compos Struct 2014;107:711–25.

[29] Bertolesi E, Carozzi FG, Milani G, Poggi C. Numerical modeling of fabric reinforce cementitious matrix composites (FRCM) in tension. Constr Build Mater 2014;70:531–48.

[30] Grande E, Ghiassi B, Imbimbo M. Chapter 19 - theoretical and FE models for the study of the bond behavior of FRCM systems. In: Ghiassi B, Milani G, editors. Numerical Modeling of Masonry and Historical Structures. Woodhead Publishing; 2019. p. 685–712. https://doi.org/10.1016/B978-0-08-102439-3.00019-1.

[31] Scacco J, Ghiassi B, Milani G, Lourenço PB. A fast modeling approach for numerical analysis of unreinforced and FRCM reinforced masonry walls under out-of-plane loading. Compos B Eng 2020;180:107553. https://doi.org/10.1016/j.compositesb.2019.107553.

[32] Scacco J, Milani G, Lourenço PB. A micro-modeling approach for the prediction of TRM bond performance on curved masonry substrates. Compos Struct 2021;256:113065. https://doi.org/10.1016/j.compstruct.2020.113065.

[33] Kumar A, Sain T. Phase field-based cohesive zone approach to model delamination in fiber-reinforced polymer composites. Compos Struct 2024;329:117751. https://doi.org/10.1016/j.compstruct.2023.117751.

[34] Raghu P, Rajagopal A, Jalan SK, Reddy JN. Modeling of brittle fracture in thick plates subjected to transient dynamic loads using a hybrid phase field model. Meccanica 2021;56(6):1269–86. https://doi.org/10.1007/s11012-020-01224-z.

[35] Cepero-Mejías F, Curiel-Sosa JL, Blázquez A, Yu TT, Kerrigan K, Phadnis VA. Review of recent developments and induced damage assessment in the modelling of the machining of long fibre reinforced polymer composites. Compos Struct 2020;240:112006.

[36] Alessi R, Freddi F. Phase-field modelling of failure in hybrid laminates. Compos Struct 2017;181:9–25. https://doi.org/10.1016/j.compstruct.2017.08.073.

[37] Donnini J, Chiappini G, Lancioni G, Corinaldesi V. Tensile behaviour of glass FRCM systems with fabrics' overlap: Experimental results and numerical modeling. Compos Struct 2019;212:398–411. https://doi.org/10.1016/j.compstruct.2019.01.053.

[38] Pagani A, Enea M, Carrera E. Quasi-static fracture analysis by coupled three-dimensional peridynamics and high order one-dimensional finite elements based on local elasticity. Int J Numer Meth Eng 2022;123(4):1098–113. https://doi.org/10.1002/nme.6890.

[39] Shen J, Arruda MRT, Pagani A. Concrete damage analysis based on higher-order beam theories using fracture energy regularization. Mech Adv Mater Struct 2023;30(22):4582–96. https://doi.org/10.1080/15376494.2022.2098430.

[40] Shen J, Arruda MRT, Pagani A, Carrera E. A regularized higher-order beam elements for damage analysis of reinforced concrete beams. Mech Adv Mater Struct 2024;31(1):79–91. https://doi.org/10.1080/15376494.2023.2245825.

[41] Misseri G, Stipo G, Rovero L. Bond behaviour of PBO FRCM on curved masonry substrates. In: Ilki A, Ispir M, Inci P, editors. 10th Int. Conf. FRP Compos. Civ. Eng., Cham: Springer International Publishing; 2022. p. 2060–72.

[42] Bertolesi E, Fagone M, Grande E, Milani G, Innovative RT, Sensor FO, et al. IEEE int. Work Metrol Living Environ 2022;2022:144–8. https://doi.org/10.1109/MetroLivEnv54405.2022.9826951.

[43] Rotunno T, Fagone M, Grande E, Milani G. FRCM-to-masonry bonding behaviour in the case of curved surfaces: experimental investigation. Compos Struct 2023;313:#116913. https://doi.org/10.1016/j.compstruct.2023.116913.

[44] Malena M, de Felice G. Debonding of composites on a curved masonry substrate: Experimental results and analytical formulation. Compos Struct 2014;112:194–206. https://doi.org/10.1016/j.compstruct.2014.02.004.

[45] Misseri G, Rovero L, Stipo G, Barducci S, Alecci V, De Stefano M. Experimental and analytical investigations on sustainable and innovative strengthening systems for masonry arches. Compos Struct 2019;210:526–37. https://doi.org/10.1016/J.COMPSTRUCT.2018.11.054.

[46] Malena M. Closed-form solution to the debonding of mortar based composites on curved substrates. Compos Part B Eng 2018;139:249–58. https://doi.org/10.1016/J.COMPOSITESB.2017.11.044.

[47] Grande E, Milani G. Modeling of FRCM strengthening systems externally applied on curved masonry substrates. Eng Struct 2021;233:#111895. https://doi.org/10.1016/J.ENGSTRUCT.2021.111895.

[48] Grande E, Bertolesi E, Milani G, Rotunno T, Fagone M. Curved masonry supports strengthened with TRM materials: advanced FE modelling. AIP Conf Proc 2022;2611:#080006. https://doi.org/10.1063/5.0120590.

[49] Castellano A, Fraddosio A, Oliveira DV, Piccioni MD, Ricci E, Sacco E. An effective numerical modelling strategy for FRCM strengthened curved masonry structures. Eng Struct 2023;274:115116. https://doi.org/10.1016/J.ENGSTRUCT.2022.115116.

[50] Grande E, Fagone M, Rotunno T, Milani G. Modeling of shear-lap tests of flat and curved masonry specimens strengthened by FRCM. Structures 2023;52:437–48.

[51] Pingaro N, Milani G. Simple non-linear numerical modelling of masonry arches reinforced with SRG using elasto-fragile and elasto-ductile truss finite elements. Eng Struct 2023;293:116637. https://doi.org/10.1016/j.engstruct.2023.116637.

[52] Grande E, Milani G, Sacco E. Modelling and analysis of FRP-strengthened masonry panels. Eng Struct 2008;30(7):1842–60. https://doi.org/10.1016/j.engstruct.2007.12.007.

[53] Pari M, Swart W, van Gijzen M, Hendriks M, Rots J. Two solution strategies to improve the computational performance of sequentially linear analysis for quasi-brittle structures. Int J Numer Meth Eng 2020;121:2128–46. https://doi.org/10.1002/nme.6302.

[54] Yu C, Hoogenboom PCJ, Rots JG. Incremental sequentially linear analysis to control failure for quasi-brittle materials and structures including non-proportional loading. Eng Fract Mech 2018;202:332–49. https://doi.org/10.1016/j.engfracmech.2018.07.036.

[55] Milani G. Semi-analytical mechanical model for FRCM-to-substrate shear bond tests. Compos B Eng 2023;266:110983.